Naval Research Laboratory
Washington, DC 20375-5320

U.S. NAVAL RESEARCH LABORATORY

NRL/6720/MR—2022/1

Plasma Kinetics of the NRL High Efficiency Electron-Beam-Pumped Argon Fluoride Laser

DR. TZVETELINA PETROVA
JOHN GIULIANI
ARATI DASGUPTA

Radiation Hydrodynamics Branch
Plasma Physics Division

MATTHEW WOLFORD
MATTHEW MYERS
ANDREW SCHMITT
STEPHEN OBENSCHAIN

Laser Plasma Branch
Plasma Physics Division

GEORGE PETROV

Directed Energy Physics Branch
Plasma Physics Division

MALCOLM MCGEOCH

PLEX LLC
Fall River, MA

October 21, 2022

REPORT DOCUMENTATION PAGE

Form Approved
OMB No. 0704-0188

1. REPORT DATE *(DD-MM-YYYY)*	**2. REPORT TYPE**	**3. DATES COVERED** *(From - To)*
21-10-2022	NRL Memorandum Report	January 2019 – September 2022

4. TITLE AND SUBTITLE

Plasma Kinetics of the NRL High Efficiency Electron-Beam-Pumped Argon Fluoride Laser

5a. CONTRACT NUMBER

5b. GRANT NUMBER

5c. PROGRAM ELEMENT NUMBER
61553N

6. AUTHOR(S)

Tzvetelina B. Petrova, Matthew F. Wolford, Matthew C. Myers, George M. Petrov, John L. Giuliani, Arati Dasgupta, Malcolm McGeoch*, Andrew J. Schmitt, and Stephen P. Obenschain

5d. PROJECT NUMBER

5e. TASK NUMBER

5f. WORK UNIT NUMBER
4892

7. PERFORMING ORGANIZATION NAME(S) AND ADDRESS(ES)

Naval Research Laboratory
4555 Overlook Avenue, SW
Washington, DC 20375-5320

8. PERFORMING ORGANIZATION REPORT NUMBER

NRL/6720/MR--2022/1

9. SPONSORING / MONITORING AGENCY NAME(S) AND ADDRESS(ES)

Naval Research Laboratory
4555 Overlook Ave, SW
Washington, DC 20375-5320

Advanced Research Projects Agency - Energy
U.S. Department of Energy
1000 Independence Ave SW
Washington, DC 20585

10. SPONSOR / MONITOR'S ACRONYM(S)

11. SPONSOR / MONITOR'S REPORT NUMBER(S)

12. DISTRIBUTION / AVAILABILITY STATEMENT

DISTRIBUTION STATEMENT A: Approved for public release; distribution is unlimited.

13. SUPPLEMENTARY NOTES

*PLEX, LLC, 275 Martine St Files / Admin, Fall River, MA 02723

14. ABSTRACT

The U.S. Naval Research Laboratory (NRL) is the world leader in the development of high-energy excimer laser science and technology [S. P. Obenschain, et al., Appl. Optics 54 (2015) 103-122]. The ArF* laser is being scaled in power and energy to become a potential direct or indirect driver for inertial confinement fusion (ICF) [Obenschain et al., Phil. Trans. R. Soc. A 378 (2020) 0031]. The research efforts are focused on combined experimental and theoretical investigation of the current ArF* technology on Electra e-beam facility. We report on modeling results from the Orestes suit of codes that includes 0D electron kinetics, 1D plasma chemistry, 1D lasing amplification, and 3D radiation transport. Laser yield, amplified spontaneous emission, small signal gain, and saturated laser intensity and their dependence on the e-beam power deposition in the range 0.5-2 MW/cm3, gas pressure 0.8-1.4 atm, and gas composition 0.1-0.5 % of F2 have been investigated. The optimum conditions for laser generation have been determined from simulations. Experimentally, laser yield as high as 200 J has been obtain on the Electra [submitted to Phys. Plasmas]. These studies pave the way for building high efficiency ArF* laser for ICF.

15. SUBJECT TERMS

Excimer Laser, Pulsed Power, Electron Beam Diode, Modeling and Simulation, Kinetics, Plasma Physics, Laser Gain, Intrinsic Efficiency, Amplified Spontaneous Emission, Laser Plasma Instabilities

16. SECURITY CLASSIFICATION OF:			**17. LIMITATION OF ABSTRACT**	**18. NUMBER OF PAGES**	**19a. NAME OF RESPONSIBLE PERSON**
					Matthew Wolford and Tzvetelina Petrova
a. REPORT	**b. ABSTRACT**	**c. THIS PAGE**	U	35	**19b. TELEPHONE NUMBER** *(include area code)*
U	U	U			202-767-3528 and 202-767-3169

Standard Form 298 (Rev. 8-98)
Prescribed by ANSI Std. Z39.18

This page intentionally left blank.

CONTENTS

This page intentionally left blank.

EXECUTIVE SUMMARY

The U.S. Naval Research Laboratory (NRL) is the world leader in the development of high-energy excimer laser science and technology [S. P. Obenschain, *et al.*, Appl. Optics **54** (2015) 103-122]. The ArF^* laser is being scaled in power and energy to become a potential direct or indirect driver for inertial confinement fusion (ICF) [Obenschain *et al.*, Phil. Trans. R. Soc. A **378** (2020) 0031]. The research efforts are focused on combined experimental and theoretical investigation of the current ArF^* technology on *Electra e*-beam facility. We report on modeling results from the *Orestes* suite of codes that includes 0D electron kinetics, 1D plasma chemistry, 1D lasing amplification, and 3D radiation transport. Laser yield, amplified spontaneous emission, small signal gain, and saturated laser intensity and their dependence on the *e*-beam power deposition in the range 0.5-2 MW/cm^3, gas pressure 0.8-1.4 atm, and gas composition 0.1-0.5 % of F_2 have been investigated. The optimum conditions for laser generation have been determined from simulations. Experimentally, laser yield as high as 200 J has been obtain on the *Electra* [submitted to Phys. Plasmas]. These studies pave the way for building high efficiency ArF^* laser for ICF.

This page intentionally left blank.

PLASMA KINETICS OF THE NRL HIGH EFFICIENCY ELECTRON-BEAM PUMPED ARGON FLUORIDE LASER

1. INTRODUCTION

1.1 NRL efforts: overview

Excimer lasers are high-power and high-efficiency coherent UV light sources [1]. A $KrF*$ laser with wavelength of 248 nm and kJ output energy was developed and continuously investigated in the past decades on the *Nike* system at the U.S. Naval Research Laboratory (NRL) [2, 3, 4, 5, 6, 7]. The *Electra* electron beam (*e*-beam) pumped laser at NRL [8] has similar architecture as *Nike* and was originally optimized to work with $Ar/Kr/F_2$ mixture, for which conversion efficiency of 12 % and net amplifier efficiency of ~7.8 % have been achieved [3]. Numerical modeling was used to guide experiments and improve system design [9], [10], [11]. The latter includes both kinetics and 3D ASE (amplified spontaneous emission) modeling of the $KrF*$ laser, and calculates laser parameters such as excitation efficiency, laser output and gain. Important aspects of these calculations are the spatial dependence of the non-saturable absorption and radiation transport accounting for mirrors reflection, cavity aspect ratio [11] and optical pulse shaping [12]. Recently, there has been renewed interest in another mixture as a laser medium, Ar/F_2, based on several factors: (i) it is the deepest UV laser (wavelength of 193 nm), that could be scaled to high energy and power; (ii) it has a broad bandwidth (5-10 THz) that enables to reach high power on nanosecond (ns) timescales; (iii) it has higher intrinsic efficiency then other excimer lasers. With all these attributes, the ArF^* excimer laser could be a superior direct and indirect driver for inertial confinement fusion (ICF). This is supported by recent results from one-dimensional simulations with the FASTRAD3D radiation hydro-code by Bates *et al.* [13] showing an ablation pressure increase and lowering of the two plasmon instability threshold when using shorter wavelength lasers [14].

1.2 Experiments: historical overview

$ArF*$ excimer laser systems have been investigated since the late seventies. However, these investigations are limited in number compared to the corresponding *KrF** studies. The ones, pertaining to *e*-beam generated plasmas, *i.e.* Ref. 15, 16, 17, 18, 19, 20, 21, 22, 23, 24, 25, 26, 27, [28, 29, 30, are summarized in Table 1 together with a historical overview. In this work, the plasma kinetics and lasing of an *e*-beam pumped ArF^* laser are modeled and compared against experimental data from the *Electra* facility ([29] and [30]). The highest gain of 200 J was obtained in oscillator mode at *e*-beam power of 0.76 MW/cm^3, pulse duration of 140 ns, with an electron beam dimensions 14x30x100 cm and extracted laser aperture of 11x30 cm^2 [31]. The progress in modeling has been reported in several conferences [32] and technical notes [33]. Together with Ar_2F^* lasing at 290 nm, this excimer laser could be potentially tunable to other wavelengths [34].

Manuscript approved October 14, 2022.

Table 1 — Historical overview on the *e*-beam pumped ArF^* laser technology research and publications: experimental conditions, yield, and reported conversion efficiency. Experimental data for *Electra* are listed in the last three rows.

Research, conditions, and yield:	**Gas mixture and pressure:**	**Intrinsic efficiency**	**References:**
Experiments, *oscillator*: 300 ns *e*-beam, 1.25 MW/cm^3 *Modeling:* quenching of $ArF^*(\,^2\Sigma_{1/2})$	Ar/F_2 0.5-4 atm Ar /2-20 Torr F_2	not published	Rokni-1977 [15]
Experiments, *oscillator*: 55 ns axial *e*-beam, yield = 92 J	Ar/F_2 1.84 atm	3 %	Hoffman-1976 [16]
Experiments, *oscillator*: 60 ns *e*-beam, 1.5 MW/cm^3, yield = 33 *J*	$Ne/He/Ar/F_2$ 3.6 atm	6 % intrinsic, 11 % peak power	Edwards-1980 [19]
Experiments, *oscillator*: 50 ns *e*-beam, 1.4 MW/cm^3,	$Ne/Ar/F_2$ 4.0 atm	4.4 % intrinsic	Suda-1985 [20]
Experiments, *oscillator*: 65 ns *e*-beam, 2.3 MW/cm^3, yield = 95 J	Ar/F_2 0.85 atm	3.4 % intrinsic	Suda-1988 [22]
Experiments, *oscillator*: 160 *ns e*-beam, > 0.3 MW/cm^3	$Ar/Ne/F_2$ 1.84 atm	7.7 % intrinsic, 11 % at peak power	Mandl-1986 [23]
Experiments, oscillator: 40 *ns e*-beam, yield = 0.13 *J*	$Ne\text{-}Ar(2\%)\text{-}F_2$ 0.98-13.8 atm	3 %	Peters-1987 [24]
Modeling and experiments: single pass amplifier 65 *ns e*-beam, 0.1-2.0 MW/cm^3	$Ar/Ne/F_2$ and Ar/F_2 mixtures 1.0 *atm*	15.5 %	Lee-1988 [25] Lee-1989 [26]
Experiments, oscillator: 1 μs *e*-beam, yield = 0.29 *J*	$Ar/Ne/F_2$ 4.0 *atm*	1.35%	Glessner-1991 [27]
Modeling: 80 *ns e*-beam	Ar/F_2 2.5-4.0 *atm*	10.4 to 23 %	Boĭchenko-1992 [28]
Experiments and modeling: double pass oscillator 140 *ns e*-beam, 0.7-0.9 MW/cm^3 maximum yield = 137 *J*	99.71% Ar/0.29% F_2 12 *psi* (0.82 *atm*)	17.7 % *Single pass amplifier efficiency (see equation (15))	Myers-2019 [29]
Experiments: quadrupole pass oscillator 140 *ns e*-beam, 0.7-0.9 MW/cm^3 maximum yield = 96 *J*	99.7%Ar/0.3% F_2 12-20 *psi* (0.95-1.36 *atm*)	8.2 % *Not accounting for optical losses	Wolford-2020 [30]
Experiments and modeling: oscillator 140 *ns e*-beam, 0.76 MW/cm^3 maximum yield = 200 *J*	99.5%Ar/0.5% F_2 13 psi (0.88 *atm*)	9.5 % *Not accounting for optical losses	2021 [31]

2. PLASMA KINETICS MODELING OF THE ARF LASER

The formation and quenching kinetics of ArF^* excimer molecule was studied in the late 70's in the pioneering work of Rokni *et al.* [15,16,17]. The most comprehensive model of laser amplifier was later developed by Lee *et al.* [26]. In this model, the electron kinetics is based on electron energy distribution function (EEDF), which is Maxwellian for the secondaries and a delta function at beam energy electrons.

A set of collisional excitation and ionization rates was calculated and used to solve a system of species balance equations along the laser direction in which extensive plasma chemistry is included. For single pass amplifier in Ar/F_2 mixture at 1.0 *atm*, the laser parameters, such as intensity amplification, small signal gain, saturation intensity, and the large signal gain were calculated. Another kinetics model for both *e*-beam and discharge pumped $ArF*$ lasers was developed by Boĭchenko *et al.* [28]. It solves the species balance equations and uses the homogeneous radiation approximation for Ar/F_2 and $Ar/Ne/F_2$ mixtures for total pressures of up to 4 *atm*, power deposition 0.1-2.4 MW/cm^3 and 65 *ns* e-beam pulse length. The most intriguing prediction made by Boĭchenko's model was that the conversion efficiency into lasing can be as large as 23 %.

Our approach includes the following physics: electron kinetics coupled with plasma chemistry for atomic, molecular, and ion species, calculated by a 1D time-dependent system of balance equation for the plasma constituents. A spatially-averaged Boltzmann code [35] provides rates for all reactions involving electrons: collisional excitation and de-excitation, attachment and detachment of electrons to fluorine atoms and molecules, and production of radical species in an ArF^* lasing medium as a function of two parameters: reduced *e*-beam power, P_{BEAM}/p, and fluorine concentration, x. Here, P_{BEAM} is the *e*-beam peak power per unit volume and p is the total gas pressure. These rates are incorporated into a 1D-hydro code that solves the species balance equations. As a result, the time- and axial-dependent species densities are obtained, which are used to model the collisional and radiative processes responsible for the upper lasing level $ArF^*(B)$ population and destruction. The population rate of the upper laser level, $ArF^*(B)$, then enters a 1D laser code and a 3D ASE numerical model, in which the radiation fluxes and output laser intensity are calculated. The Boltzmann treatment of electron kinetics and the 3D ASE are the main distinction between our model the ones listed in the previous paragraph.

For the electron kinetics, the electron energy distribution function was numerically calculated by solving the 0D steady-state Boltzmann equation and the rates of individual processes, such as electron collisional excitation, ionization and dissociation, were calculated for various fluorine concentrations in argon and reduced *e*-beam power [35]. These rates, together with extensive plasma chemistry rates, are included in a system of balance equations for the following species: *electrons*, Ar and F (0.82 eV) atoms, Ar_2 molecules in ground state, atomic excited states $Ar*$ (11.65 eV), $Ar**$ (13.17 eV), and F^*(12.7 eV), molecular electronically excited states Ar_2^* (10.6 eV), F_2^*, (11.57 eV), $ArF^*(B)$ (8.3 eV), $ArF^*(C)$ (8.3 eV), Ar_2F^* (6.0 eV), atomic ions Ar^+ (15.76 eV) and F^- (-2.58 eV), and molecular ions Ar_2^+ (14.53 eV) and F_2^+ (15.69 eV). In this model we carry the four $4s$ levels as a block of levels denoted as $Ar*$ by lumping the fine structure sub-levels weighted by the *g*-factors. Analogously, $Ar**$ is a lumped block of the ten $4p$ levels. The threshold energies or enthalpies for all species are listed in the brackets. For reader's convenience, they are also listed in the **Appendix, Table 1**.

2.1 Model overview

In this subsection, we provide an overview of *Orestes*.

2.1.1 Electron kinetics

It is well-known that high-energy *e*-beams (100's of KeV) form plasma with complex electron energy distribution function that extends up to the *e*-beam energy. Collisional rates with electrons can be calculated accurately with the EEDF, which is obtained by solving the electron Boltzmann equation. The EEDF is used to calculate the following rates: (i) elastic collisions with Ar, F, and F_2; (ii) electron impact excitation of *Ar*, *F* and F_2; (iii) *e*-beam, electron impact and Auger ionization; (iv) dissociation, vibrational excitation and attachment to F_2, and (v) dissociative recombination. The electron collisional impact rates from the ground state were calculated as function of *e*-beam power per unit volume, P_{BEAM} , total pressure *p*, and gas composition. Then, the collisional rates were fitted as a function of fluorine concentration and reduced *e*-beam power $\bar{P} = \frac{2P_{BEAM}\,[MW/cm^3]}{p[atm]}$. The total collisional ionization rate R_{BEAM}^{ion} is put in the familiar form using the calculated energy per electron-ion pair, W_{ei} ,

$$R_{BEAM}^{ion}(\bar{P},x,z,t)=\frac{P_{BEAM}\,(t)}{W_{ei}(z,x,t)} \tag{1}$$

and partitioned among direct ionization, electron impact dissociative ionization, and Auger ionization. The excitation rates $R_{Ar(4s)}^{exc}$ and $R_{Ar(4p)}^{exc}$ are expressed through the ionization rates using the excitation-to ionization ratios $\eta_{Ar(4s)}^{exc}(x)$ and $\eta_{Ar(4p)}^{exc}(x)$:

$$R_{Ar(4s)}^{exc}(\bar{P},x,z,t)=\eta_{Ar(4s)}^{exc}(x)R_{BEAM}^{ion}(\bar{P},x,z,t) \tag{2a}$$

$$R_{Ar(4p)}^{exc}(\bar{P},x,z,t)=\eta_{Ar(4p)}^{exc}(x)R_{BEAM}^{ion}(\bar{P},x,z,t). \tag{2b}$$

The collisional rates of electrons with F_2 are also approximated as functions of $\bar{P}$ and x [35], where x is the concentration of F_2 in the Ar/F_2 mixture. The above rates are calculated at any time t and spatial position along the lasing direction, z. A list of rates is provided in **Appendix, Table A2.**

Collisional processes such as stepwise ionization or excitation between Ar^* and Ar^{**} have low energy threshold, comparable to the electron temperature T_e. For these processes, the rates are calculated with a Maxwellian EEDF and written in Arrhenius form

$$R(z,t)=AT_e^{\eta}(z,t)e^{-b/T_e(z,t)}. \tag{3}$$

with fitting parameters A, b, and η.

The lowest energy part of the EEDF is approximated with a Maxwellian for the purpose of calculating the temperature of the bulk of electrons, T_e. This is done by solving the electron energy balance equation

$$\frac{\partial}{\partial \mathrm{t}}\left(\frac{3}{2}n_e(z,t)k_BT_e(z,t)\right)=P_{BEAM}\,(t)+\sum_s\Bigg(P_s^{chem}(\bar{P},x,z,t)-P_s^{ion}(\bar{P},x,z,t)-$$

$$P_s^{exc}(\bar{P},x,z,t)-\frac{3m_e}{m_s}n_e(z,t)\nu_{es}k_B\left(T_e(z,t)-T_g(z,t)\right)\Bigg). \tag{4}$$

In Equation (4), n_e is the electron density, k_B is the Boltzmann constant, ν_{es} is electron-neutral collision frequency, m_e and m_s are the mass of electrons and species s, respectively, and P is the power gain or loss due to collisions. Subscript s denotes species and the superscript denotes the corresponding process. The initial condition for solving Equation 4 is $T_{e,0}(z)=0.03\ eV$. An analogous equation is used for the gas temperature.

Other collisional data with electrons included in the kinetics model are: electron impact excitation (Refs. [26] and [36]); de-excitation with rates estimated by McGeoch [33] using Vriens and Smeets review [37]; electron impact ionization [26]; dissociative recombination [38]; superelastic electron dissociation [26]; electron attachment and inelastic dissociative attachment, electron impact dissociation [26]; and 3-body recombination [39]. A list of rates is provided in **Appendix, Table A3.**

2.1.2 1D collisional radiative model

There are other reactions included in the kinetic model, which are relevant to heavy species:. neutral-neutral reactions [33, 40], Penning ionization [41] and [42], ion charge transfer reactions, ion charge transfer [43], and ion-ion recombination. For the latter, density effect [44], gas temperature [45] and plasma shielding [46] have been taken into account. The full list of reactions used in this work is provided in **Appendix, Table A4.**

The plasma chemistry module defines species, rate constants, rates, rate equations, and partial contribution of each reaction in the rate equations. Also, data mapping is performed in order to accommodate the different dimensionality of *Orestes* subroutines. For example, species densities mapping transfers data from the 1D chemistry code (collisional-radiative model) to the 3D radiation code.

2.1.3 Vibrational excitation of ArF molecule and radiation*

One of the most important futures of the excimer molecules is their electronic structure: a covalently bounded ground state $^2\Sigma^+$ (^1S ground state of argon and ^2P ground state of fluorine atoms at infinite inter-nuclear separation) and ionically bound, charge transfer state (correlating ^2P of Ar^+ and ^1S of the halogen negative ion, F^-, at infinite inter-nuclear separation) [1]. Hartree-Fock self-consistent-field calculations for ArF (ground and electronically excited $^2\Pi$ states) energy curves are given in Ref. [47]. In Ref. [48] and [49] an *ab initio* study of some noble gas-monohalides are performed and potential energy curves are computed including for ArF^*. From Tables II and VIII in Ref. [49], the following quantities relevant to the lasing transition $2\,^2\Sigma^+ \rightarrow X\,^2\Sigma^+$ are used: emission energy 6.49 eV and Einstein *A*-coefficient $A = 2.67 \times 10^{-8}\ s^{-1}$ (lifetime $\tau = 2.7\ ns$). For modeling the ArF^* molecule, rigid rotator model is used in *Orestes* with parameters $\omega_B = 390\ cm^{-3}$ and $\omega_{BX} = 2.7\ cm^{-3}$ [49]. The number of vibrational levels is 51 and the spacing between B and C levels of the *ArF* molecule is $\Delta E = E_B - E_C = 120\ cm^{-1}$.

2.1.4 Stimulated and spontaneous emission at 193 nm, radiative rates and gain equation 1

The deep VUV light at 193 nm is generated in the entire volume pumped by the *e*-beam and gets amplified in the laser cavity. The first analysis of the ASE was performed by Rigrod [50], who included homogeneous line broadening and an average non-saturable loss coefficient. Later, in Ref. [51], an one-dimensional numerical model for single and double pass amplifiers was developed. In general, the radiation transport module accounts for spontaneous radiative decay and stimulated emission of ArF^* molecules using the following equation:

$$(c^{-1}\partial_t \pm \partial_z) I_{\pm}(\boldsymbol{r}, \nu, t) = [g(\boldsymbol{r}, \nu, t) - \alpha(\boldsymbol{r}, \nu, t)] I_{\pm}(\boldsymbol{r}, \nu, t), \tag{5}$$

with gain coefficient $g(\boldsymbol{r}, \nu, t)$ and absorption coefficient $\alpha(\boldsymbol{r}, \nu, t)$. The gain coefficient $g(\boldsymbol{r}, \nu, t) = N_{ArF^*}(\boldsymbol{r}, t)\sigma(\nu)$ is proportional to the upper level density, $N_{ArF^*}(\boldsymbol{r}, t)$, and the stimulated emission cross section, $\sigma(\nu)$, with ν being the line profile frequency. For the KrF^* laser in oscillator mode, the most comprehensive study of was performed by Rice *et al.* [52], where the effects of transmissions from windows and unpumped regions at the laser wavelength are accounted for in the laser propagation equation.

The amplified spontaneous emission module for high gain KrF^* laser amplifier in *Orestes* includes 3D numerical modeling of ASE and parasitic oscillations. A detailed discussion regarding the numerical technique to solve the radiation transport equation is provided in Ref. [11]. Here, we describe a model for ArF^* single pass amplifier at the central laser frequency. It is based on the following system of equations. The first equation is for the laser intensity propagation in axial direction:

$$\frac{dI}{dz} = I(g - \alpha), \tag{6}$$

where

$$g \equiv \sigma N_{ArF*(B)} \equiv \frac{g_0}{1 + \frac{I}{I_{SAT}}} \tag{7}$$

is the large signal gain, g_0 is the small signal gain, and I_{SAT} is the saturated laser intensity. They are defined as

$$g_0 \equiv \sigma G_{ArF*(B)} \tau_{\mathrm{ArF*(B)}} \tag{8}$$

$$I_{SAT}(\nu) \equiv \frac{h\nu}{\sigma_{se}\tau_{ArF*(B)}}, \tag{9}$$

where $G_{ArF^*(B)}(z,t)$ is the production rate and $\tau_{ArF^*(B)}$ is the effective lifetime, including spontaneous emission and collisional quenching, and $h\nu$ is the energy of the lasing photon. The population of the upper lasing level, ArF*(B), is calculated by solving the time-dependent species balance equation on the laser axis:

$$\frac{d\,N_{ArF*(B)}(z,t)}{dt} = G_{ArF*(B)}(z,t) - N_{ArF*(B)}\left(\frac{1}{\tau_{ArF^*(B)}} + \frac{\sigma_{se}I}{h\nu}\right). \tag{10}$$

The last term in the right hand side is the stimulated emission rate with photoabsorption cross section σ_{se}, which for various species is listed in Table 2 [33, 53, 54, 55, 56].

Table 2 Photoabsorption cross sections at λ=193 nm for various species used in Orestes.

Species:	Cross sections (cm^2):	References:
F_2	1.0×10^{-21}	Argüello-1995
Ar^*	3.5×10^{-20}	Duzy-1980
Ar^{**}	3.0×10^{-18}	Duzy-1980
Ar_2^*	6.3×10^{-19}	Sauerbrey-1987
Ar_2F^*	5.0×10^{-19}	McGeoch-2017
Ar_2^*	1.0×10^{-19}	NRL estimate
F^-	6.5×10^{-18}	Mandl-1971

For all other species *s*, the rate balance equations are:

$$\frac{dN_s(z,t)}{dt} = G_s(z,t) - L_s(z,t), \tag{11}$$

where $G_s(z,t)$ and $L_s(z,t)$ are gain and loss terms. The main distinction between (10) and (11) is the lack of the stimulated emission rate term, $\sigma_{se}I/h\nu$, which affects only the ArF* (B) state. We carry about 70 plasma chemical reactions for 15 species in the model. For each reaction, the rate, threshold energy, and heat capacity are provided in order to solve the rate equations and the energy balance equations for electrons and heavy species self-consistently.

2.1.5 Model geometry

*Electra'*s main components are shown Ref. [57]. Here, in **Fig. 1,** we provide a sketch of the geometry that is used for most of the computations in this work. The *e*-beam pumped volume is 879 liters, filled with a mixture of Ar and F_2 gas at specified pressure. Two counter-propagating *e*-beams from each side of the laser cavity and perpendicular to axis *z* pump the volume. A lasing is produced along z via the chain of reactions:

$$e\text{-}beam + Ar + F_2 \rightarrow \cdots \rightarrow ArF^*(B) \rightarrow Ar + F_2 + h\nu(193nm). \tag{12}$$

The rear and front windows with transmissions T_{wm} and T_{wc}, rear mirror and output coupler/mirror reflectivity, as well as non-pumped buffer gas regions are included in the gain analyses. This geometry allows to work with only part of the volume for high lasing performance, as well as different configurations, as described in Ref. [30], where a quadrupole pass oscillator using four mirrors lead to a large laser output of 137 J.

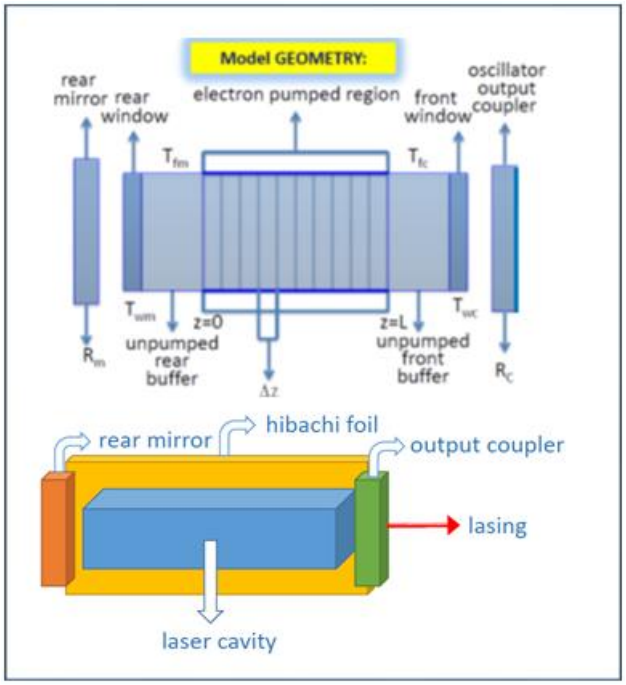

Fig.1 — Model geometry for numerical simulations. The gas cavity *e*-beam pumped regions are surrounded on both sides with non-pumped buffer gas. Laser propagation accounts for rear and front windows transmissions. Rear mirror and output coupler/mirror are situated on both sides of the laser cavity. This geometry allows to work with part of the volume for high performance laser operation and the mirrors away from the damaging *e*-beams (top plot). The ASE simulations are performed in 3D geometry (bottom plot). *Electra* has a double side e-beam pumping. The Hibachi foil, shown in yellow on the bottom plot, is sketched only for the far end.

2.1.6 Numerical simulations

The *Orestes-ArF* suite of codes requires the following *input*: (i) experimental parameters such as peak beam power and beam shape in time, gas pressure and gas composition; (ii) initial densities for all species, electron and gas temperature, (iii) reactions enthalpies; (iv) vessel geometry, mirrors reflectivity, windows transmissions needed for laser and gain module; (v) data for vibrational kinetics needed for the ArF^* quantum mechanics code.

A block diagram of Orestes is given in **Fig. 2,** in which the input, equations and output are listed. Combined electron kinetics equations with 1D collisional-radiative model (CRM), laser propagation equation, and radiation transport fluxes are solved self-consistently. The code is based on finite difference discretization. The output from the electron kinetics are collisional rates with electrons as a function of *e*-beam power, total gas pressure and gas composition. These rates enter the plasma chemistry part of the model, denoted as ORESTES, which solves for the species densities along the laser axis z. Finally, the ArF^* density is mapped on a 3D grid for laser propagation and radiation transport calculations.

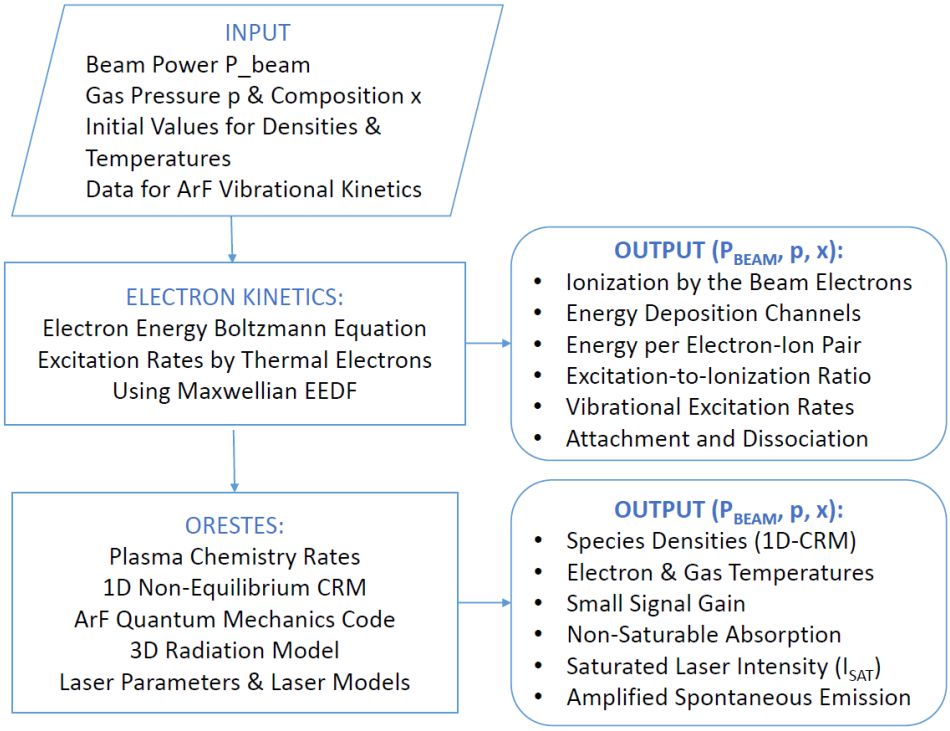

Fig. 2 —Block diagram of *Orestes-ArF** suite of codes: input data (INPUT), electron kinetics data from the EEDF, *i.e.* collisional rates with electrons (ELECTRON KINETICS), and plasma chemistry model with vibrational kinetics (*ArF** quantum mechanics code), radiation transport and laser model (ORESTES). The output is listed on the right.

2.2. Spatially-averaged populations of various species in Ar/F2 plasmas

2.2.1 Time-dependent electron beam profile

The Orestes time-dependent plasma chemistry module (CRM) is one of the major components in the *ArF** laser kinetics. It is driven by *e*-beam electrons with specified energy and current density that create secondary electrons inside the laser cavity and produce almost instantaneously a non-LTE plasma. The experimentally measured time-dependent single shot *e*-beam power per unit volume is shown in **Fig. 3**. It has a sharp rise-time of 50 ns up to 0.4 MW/cm^3, and a more gradual increase between 50 and 130 ns up to the peak power density of $P_{BEAM}^{max} = 500\ kW/cm^3$. For the next 130 ns, the *e*-beam power decreases in time. For the simulations shown in this paper, the shape of the pulse is kept the same, but the maximum *e*-beam power was varied, *i. e.* the whole pulse is scaled with *e*-beam power.

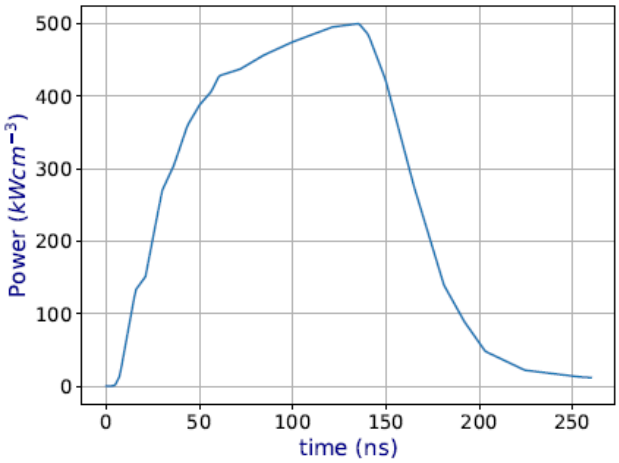

Fig. 3— Experimental *e*-beam power as function of time.

2.2.2 Species densities

In this sub-section we will discuss simulation results from the Orestes plasma chemistry module in order to get better understanding of plasma characteristics that are essential for the laser operation and determine laser parameters such as gain, amplification, and emission. Throughout we consider Ar/F_2mixture in which the fluorine concentration is low, less than 1 %. The species densities versus time are plotted in **Fig. 4** at typical operating conditions: beam power $P_{BEAM}^{max} = 0.5\ MW/cm^3$, total pressure $p = 12.5\ psi$, and F_2 concentration $x = 0.5$ %. The top panels display the densities of neutrals, the lower left panel shows the population of the upper laser level and the bottom right panel shows the electron and ion densities. The excited state $Ar*$ reaches maximum population on the order of 10^{15} cm^{-3} at time 150 ns, just after the peak of the *e*-beam pulse, and then decreases. Initially, the population of the $Ar**$ levels is proportional to the population of the $Ar*$ levels, but after the peak of the *e*-beam it drops faster than the $Ar*$ levels due to radiative processes. The maximum population is about $3 \times 10^{14} cm^{-3}$, approximately one-third of the maximum population of the $4s$ levels. The population of the argon molecular dimer, Ar_2^*, is about an order of magnitude lower than the population of $Ar*$ and follows its temporal dependence. This is because it is formed in three-body reactions from $Ar*$, *i.e.* $Ar*+Ar + Ar \rightarrow Ar_2^* + Ar$. The population of Ar_2F^* is orders of magnitude lower, but it gradually increases with time and exceeds the density of Ar_2^* at the end of the *e*-beam pulse. The initial F_2 density is set by the prescribed concentration of fluorine, but it decreases in time due to electron impact dissociation. At the end of the *e*-beam pulse, at time *t*=200 ns, F_2 is 50 % dissociated. At the same time, the atomic fluorine density, which is zero initially, keeps increasing as the reverse processes are slow. The number of dissociated F_2 molecules per unit volume is proportional to the *e*-beam energy deposition per unit volume, $\varepsilon_{BEAM} = \int_0^\infty P_{BEAM}\,(t)dt$ [35]. If ε_{BEAM} exceeds a certain critical value, F_2 molecules will be dissociated, which may put an upper limit to the energy deposition. This effect can be counteracted by adding more fluorine to the mixture.

The population of $ArF*$ excimer molecules is plotted in the lower left panel of Figure 4. Unlike the other excited states, it reaches maximum well before the peak of the *e*-beam pulse, at time *t*=50 ns. The peak value is $\sim 5 \times 10^{14} cm^{-3}$, very close to that measured in [58], which is $\sim 4 \times 10^{14} cm^{-3}$. It is notable, that in their experiments, the peak density was also reached very early in time, at *t*=40 ns, but for a discharge pumped scheme (applied voltage $V = 28\ kV$, reduced applied electric field 22 Td at total pressure 2.5 atm and gas composition $Ar/F_2/He = 89.5\% / 0.5\% / 10\%$). The mechanisms for population and destruction of $ArF*$ will be discussed later in this section in relation to the formation of population inversion and gain.

The electron and ion densities are plotted in the lower right panel of Figure 4. The peak electron density is ~$5\times 10^{14} cm^{-3}$. The dominant positive ion is Ar^+, followed by Ar_2^+. The density of F_2^+ is lower due to the small concentration of fluorine, but at the end of the *e*-beam pulse becomes comparable to the densities of Ar^+ and Ar_2^+. The density of the only negative ion considered in the model, F^-, is very large

and follows the electron density profile since it is formed in dissociative attachment to F_2 molecules, $F_2 + e \rightarrow F^- + F$, a process known from studies of the KrF*plasma kinetics [59]. It flattens at time t=30 ns to a value of $N_{F^-} = 1 \times 10^{14} cm^{-3}$. This value is somewhat less than that reported in Ref. [58] for a discharge-pumped ArF* laser ($N_{F^-} = 3 \times 10^{14} cm^{-3}$). After the peak of the laser pulse, the production rate of ions decreases and the ions are annihilated via ion-ion recombination, as well as dissociative recombination with electrons. The time scale for these processes is on the order of 100 ns.

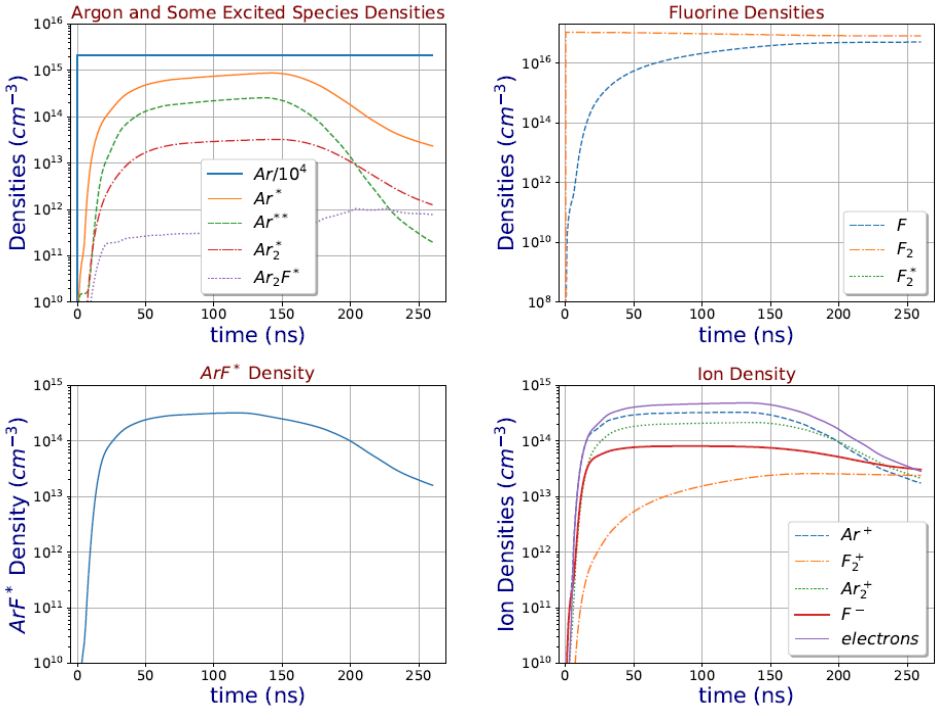

Fig. 4 — Species densities in ArF* oscillator as function of time at e-beam power 0.5 MW/cm^3, total gas pressure of 12.5 psi, and composition 0.5% of F_2 in Ar.

2.2.3 *Production and loss of ArF* molecules. Lasing mechanism*

Of critical importance for lasing is the population of the upper laser level, ArF*(B), since it determines the large signal gain given by Equation 7. Here, we will focus on the production and destruction rates due to various collisional and radiative processes. The production of ArF^* proceeds through two main channels: collisions of fluorine molecules with argon neutrals in excited states and ion-ion recombination [30]. Equally important are the loss mechanisms of ArF* molecules since they lead to decrease of lasing. They include collisional deactivation with electrons and neutrals (Ar, F_2), as well as spontaneous and stimulated emission. Next, we compare the production and loss rates and their relative contributions to population of ArF^* during the e-beam pulse.

In **Fig. 5** we plot two series of simulation results: for e-beam power of 0.5 MW/cm^3 and 1 MW/cm^3. The most effective production channel is the collisions of Ar excited atoms with fluorine molecules, the so-called harpoon reaction ($Ar^*+F_2 \rightarrow ArF^* + F$), also in Ref. [15]. For 0.5 MW/cm^3 power deposition, the rate at its maximum is $8 \times 10^{22} cm^{-3} s^{-1}$. For 1 MW/cm^3 power deposition, however, the production rate in Equation 8 is $1.8 \times 10^{23} cm^{-3} s^{-1}$, *i.e.* it exhibits a slight non-linear increase. The production of ArF^* is most effective between 50 and 180 ns, which coincides with the production of Ar* state in electron impact collisional excitation of argon atoms from the ground state. This collisional excitation rate depends on the EEDF and follows the beam power deposition plotted in **Fig. 3**.

The next important contributors to the production of ArF^* arise from the ion channel, while other reactions contribute marginally. The major losses are due to neutral collisions of ArF^* with Ar atoms and F_2 molecules, followed by super-elastic collisions with electrons and dissociative attachment. Radiation accounts for only a few percent of the total loss rate. Time-integrated relative contributions for creation and destruction of ArF^* at e-beam power deposition of 1 MW/cm^3 are listed in **Table 3.**

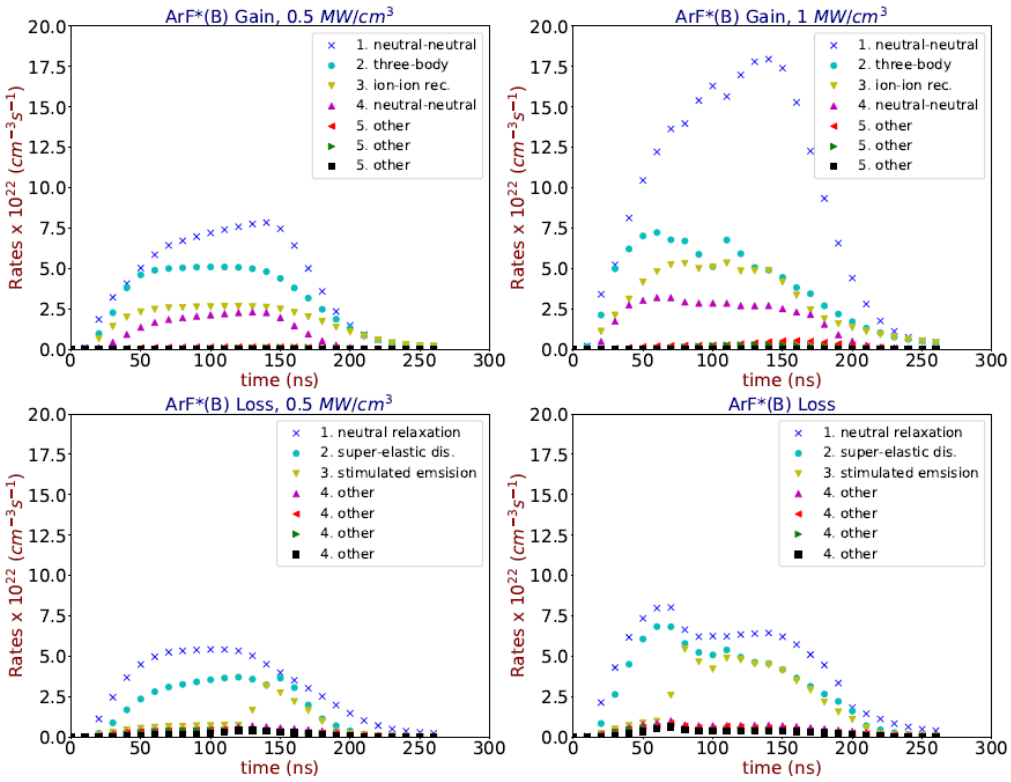

Fig. 5 — Gain and loss rates as a function of time for ArF^* oscillator at e-beam power deposition 0.5 MW/cm^3 (left) and 1 MW/cm^3 (right), total gas pressure of 12.5 psi, and composition 0.5% of F_2 in Ar.

Table 3 — Relative contribution to the gain and loss channels for ArF^* for power deposition of 1 MW/cm^3, total gas pressure of 12.5 psi, and 0.5% of F_2 in Ar.

Gain of ArF*	Reaction:	Contribution
neutral-neutral reaction	$Ar^*+F_2 \rightarrow ArF^* + F$	**43 %**
three-body reaction	$Ar_2^+ + F^- + Ar \rightarrow ArF^* + 2Ar$	**29 %**
ion-ion recombination	$Ar^+ + F^- \rightarrow ArF^*$	**15 %**
other reactions:	$Ar^*+F_2 \rightarrow ArF^* + F$ $Ar_2^* + F_2 \rightarrow ArF^* + F + Ar$ $Ar_2^* + F \rightarrow ArF^* + Ar$	**13 %**
Loss of ArF*:		
neutral relaxation	$ArF^* + F_2 \rightarrow Ar + F + F_2$:	**51%**
super-elastic dissociation	$ArF^* + e \rightarrow Ar + F + e$	**35%**
neutral relaxation	$ArF^* + Ar \rightarrow F + 2Ar$	**10%**
radiation and dissociation	$ArF^* \rightarrow Ar + F + hv_0$ $ArF^* + e \rightarrow Ar^*+F^-$ $ArF^* \rightarrow Ar + F + hv_X$ $ArF^* + hv_0 \rightarrow Ar + F + 2hv_0$	**4%**

2.2.4. Electron and gas temperature

The EEDF for *e*-beam plasmas is highly non-Maxwellian, extending up to the *e*-beam energy, U_{BEAM}. It is nonetheless convenient to use as a parameter the electron temperature, which determines the average energy of the electron bulk. The electron temperature is conventionally defined as

$$T_e = \frac{2}{3}\langle u \rangle = \int_0^{U_{BEAM}} u f(u')\, du' \tag{13}$$

by averaging the electron kinetic energy u over the EEDF $f(u)$, and $\langle u \rangle$ is the mean electron energy. *Orestes* also computes the gas temperature, T_g, from the gas thermal balance equation to account for the heating of the gas and chemical reactions rates that depend on T_g. The time evolutions of the electron and gas temperatures are plotted in **Fig. 6**. The electron temperature raises sharply (~10 ns) and remains flat at about 2 eV for the entire e-beam pulse duration. The gas temperature steadily increases from room temperature to 420 K (**Fig. 6**).

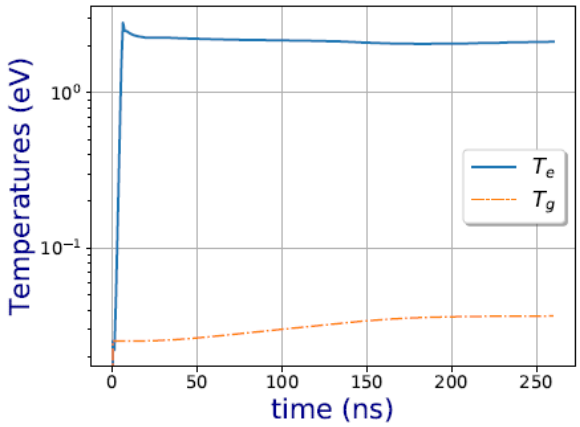

Fig. 6 — Electron and gas temperatures for ArF^* oscillator as function of time for *e*-beam power 0.5 MW/cm^3, total gas pressure 12.5 psi and composition 0.5% of F_2 in argon.

3. LASER MODELS IN ORESTES

In order to systematically study the ArF^* laser, various laser configurations on *Electra* have been explored. For single and double pass amplifiers, small signal gain measurements and calculation are discussed in Myers *et al.* [29] and [60]. For quadrupole pass oscillator results are published in Wolford *et al.* [30], where ASE and laser yield were measured using high pressure photodiode. Laser yield of 137 J was measured in laser mixture of 99.71 % Ar and 0.29 % F_2 at total pressure 14 psi. In this section, we provide a summary of these results.

3.1 Single and double pass amplifiers

In the single pass amplifier (SPA) laser configuration, a commercial discharge ArF^* laser is used as a seed laser that propagates along the z-axis. By varying its intensity, the small signal gain was determined ([29] and [60]). SAP was studied by Lee *et al.* [26] using pulse propagation equation with transient spatial and temporal dynamics for *e*-beam deposition rates in the range 0.1 to 2 MW/cm^3. The reported amplifier efficiency exceeded 10% in argon-rich mixture of $Ar/Ne/F_2$. In this sub-section we compare our results for laser parameters in SPA mode with the results from the latter reference since our investigations are performed at similar conditions.

For SPA, Giuliani [61] has developed a method for estimating the small signal gain in steady-state using the following assumptions: (i) there are no mirrors; (ii) transmission and reflection coefficient of the laser cell interfaces are assumed known. One can define the following relations:

$$\mathcal{R}_f \equiv \Upsilon_{F_2}\Upsilon_{W_2} \text{ and } \mathcal{R}_b \equiv \Upsilon_{F_1}\Upsilon_{W_1},$$

where Υ_{F_1} and Υ_{F_2} are the transmission coefficients through the sections of unpumped gas and Υ_{W_1} and Υ_{W_2} are the transmission coefficients through the cell windows. Then define the ratios

$$y(L) \equiv \frac{1}{\mathcal{R}_f}\frac{I_{OUT}}{I_{SAT}} \text{ and } y(0) \equiv \mathcal{R}_b\frac{I_{IN}}{I_{SAT}},$$

where I_{IN} is the input laser intensity (known parameter), I_{OUT} is the output laser intensity, either measured or calculated, and L the length of the gain region. The laser intensity propagation Equation 6 becomes

$$(\gamma-1)\alpha L - ln\left[\frac{y(L)}{y(0)}\right] + \gamma \ln\left[\frac{y(L)-(\gamma-1)}{y(0)-(\gamma-1)}\right] = 0. \quad (14)$$

There are five parameters in this equation: $\gamma = g_0/\alpha$, αL, I_{IN}, I_{OUT}, and I_{SAT}. We assume that αL, I_{IN}, I_{OUT}, and I_{SAT} are specified and g_0, the small signal gain, is to be determined.

To test the validity of the *Orestes* SPA model, we compare the calculated small signal gain, absorption and saturated laser intensity to experimental data obtained on *Electra* [26]. The results are plotted in **Fig. 7** as a function of *e*-beam power. From measured seed laser intensity, I_{IN} , and output laser intensity, I_{OUT}, one can estimate the small signal gain using **Formula 14**. The measured small-signal gain on *Electra* SPA was $g_0 = 12.1\ \%/cm$, absorption coefficient α~0.70 $\%/cm$ and saturated intensity $I_{SAT} = 6.6\ MW/cm^2$. The numerical results from *Orestes* show good agreement with the experiments on *Electra*. The small-signal gain, however, was considerably larger compared to that measured by Lee *et. al.* [26] due to the larger *e*-beam power deposition. In another study, a longitudinally pumped excimer amplifier at high power (~5 MW/cm^3) and short duration (15 ns FWHM) was studied experimentally [62]. The gas compositions was 953 $Torr\ Ar$ and 8 $Torr\ F_2$. (0.83 % F_2 concentration). Measured gain at 193.68 nm, away from the gain peak, was $g_0 = 10.8\ \%/cm$, absorption coefficient α~0.70 $\%/cm$ and saturated intensity $I_{SAT} = 7.9\ MW/cm^2$.

For double pass amplifier, the measured small signal gain was 3.21 %/cm, the absorption coefficient was 0.16 %/cm, and the saturation intensity was $I_{SAT} = 10\ MW/cm^2$ for total pressure 12 *psi* with 0.3 % F_2 [29]. The output laser energy was 96 J and the extraction efficiency was estimated to be $\frac{I_{OUT}-I_{IN}}{g_0 I_{SAT} L} = 26.7\%$. The intrinsic efficiency, defined as

$$\text{Intrinsic Efficiency} = \frac{\text{Laser Energy Output}}{\text{Electron Beam Energy+Seed Laser Energy}} \sim 17.7\ \%, \quad (15)$$

exceeds that of the KrF^* laser.

3.2 Double and quadrupole pass oscillators: experiments

To allow higher *e*-beam energy deposition, double and quadrupole oscillator systems have been built on *Electra*. The laser energy, time-dependent laser intensity and ASE were measured in a range of total gas pressures 0.8-1.4 atm and published in Ref.[30], where the output laser energy was measured using calorimetry and the laser intensity and ASE were measured with photodiodes. Here we list in **Table 4** some of the results from Ref. [30] for quadrupole pass oscillator. The peak power efficiency was defined as

$$Peak\ Power\ Efficiency = \frac{Peak\ Laser\ Power}{Peak\ Electron\ Beam\ Power}. \quad (16)$$

and it is between 12 and 16 % for *e*-beam power deposition in range 0.6-0.9 MW/cm^3. For this quadrupole pass configuration, models on *Orestes* were not performed.

Table 4 — Performance of quadrupole pass ArF^* oscillator at fractional gas composition 99.7% Ar, 0.3% F_2 and different total gas pressures. The highest measured yield was 96 J at 1.09 *atm* total gas pressure.

Output Laser Energy	Total pressure	Flat-top e-beam peak power	Peak power efficiency
80 J	1.36 atm (20 psia)	0.9 MW/cm^3	12 %
96 J	1.09 atm (16 psia)	0.8 MW/cm^3	14 %
90 J	0.82 atm (12 psia)	0.6 MW/cm^3	16 %

In a non-optimized dual parallel ArF^* oscillator, the maximum measured laser output energy was 137 J in

99.71% *Ar* and 0.29% F_2 at 14 *psi* (0.95 *atm*). The best agreement between experiments, 0.82 J/cm^2 over 10.5x11 cm^2 laser aperture, and Orestes, 0.84 J/cm^2, was for *e*-beam power deposition of 0.6 MW/cm^3 and total pressure of 0.82 *atm* with a fraction of 0.3% F_2 in argon. At higher pressure, the *Orestes* predicts significantly higher laser yield, which is attributed to small errors in 3-body reaction rates. The detailed kinetics modeling at high pressure will be a subject of future work.

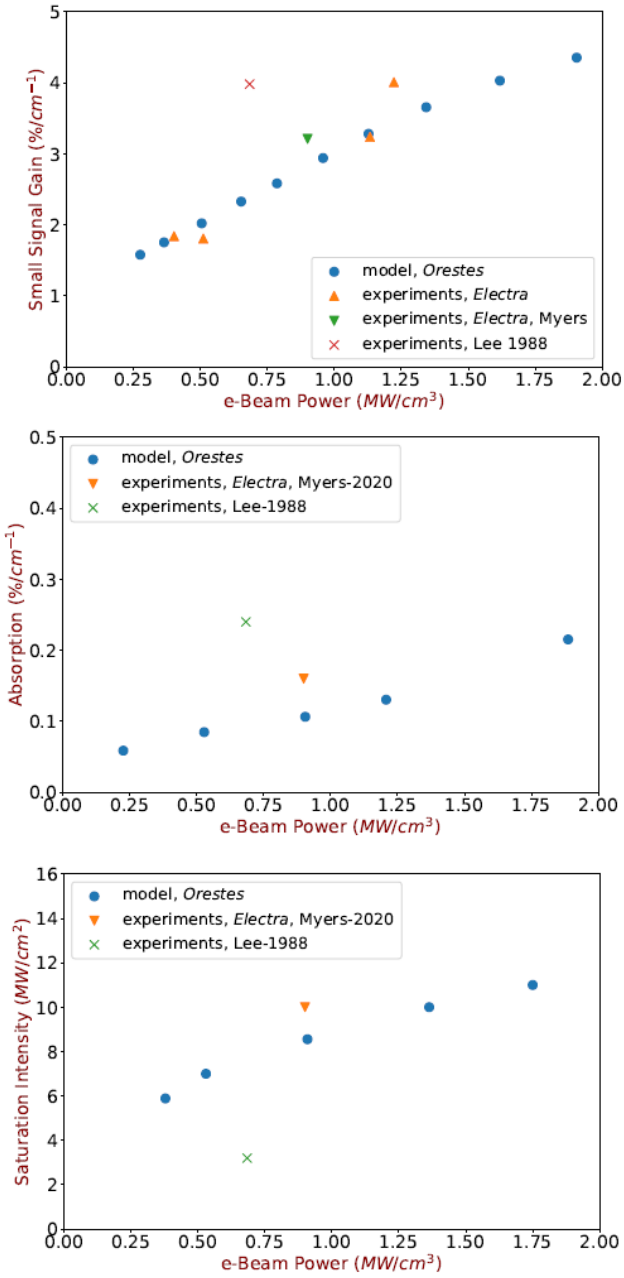

Fig. 7 — Small signal gain in *ArF** single pass amplifier (top), absorption (middle), and saturation intensity (bottom) as a function of *e*-beam power deposition. Comparison of *Orestes* numerical results with experiments on *Electra* ([29] and [60]) and experimental data from Refs. [25, 26]. The total gas pressure vary between 12 and 20 *psi* with 0.3% of F_2 in argon.

3.2 Oscillators: time-dependent absorption, small signal gain, and saturated intensity

The production and loss mechanisms of ArF^* molecules in oscillator mode were elaborated in **Section 3**. In this subsection, we will discuss the time-dependent laser characteristics (**Equations 6-12** applied for an ArF^* oscillator). All the results, shown here, are at total gas pressure 12.5 *psi* and gas composition 0.5% of F_2 in Ar.

The most important physics pertained to gain calculations is presented in **Fig. 8**. On the left panel, the coefficient $\gamma = \frac{g_0}{\alpha}$, as defined by Rice *et al.* [52], is about 17.5. The effective lifetime of the upper laser level calculated by our model is $\tau_{ArF^*(B)}$~2.4 ns, which accounts for both spontaneous emission and collisional quenching. In Ref. [52], the radiative decay rate is 2.67x10^8 s^{-1} corresponding to radiative lifetime 3.7 ns, where collisional depopulation was not considered. On the right panel, the small signal gain and absorption coefficient versus time are plotted. The small signal gain profile follows that of the *e*-beam power pulse shape. It increases and reaches maximum of 2.5 %/cm at time *t*=130 ns. The absorption coefficient, plotted with red broken line, is only 0.2 %/cm, an order of magnitude lower compared to the small signal gain. It accounts for the absorption of photons by several species such as F_2 and argon excited states, and it is defined as

$$\alpha(z,t) = \sum_s \sigma_s(h\nu_0)N_s\,(z,t), \tag{17}$$

where N_s is the species population and σ_s is the absorption cross section for species *s* at the central laser frequency $\nu_0 = c/\lambda_{LAS}$ for the laser wavelength $\lambda_{LAS} = 193\ nm$. The individual absorption cross sections are listed in **Table 2**. In order to get insight into the absorption of photons at the laser wavelength, in **Figure 9** we compare the partial contributions of different species. The strongest absorber is Ar^{**}, because it has the largest absorption cross section ($3.0 \times 10^{-18}\ cm^2$ at 193 nm). Ar^* states contribute marginally even though their population is larger, because the corresponding cross section is two orders of magnitude smaller. The second largest absorber is F_2 due to its high density that compensates for the small absorption cross-section of 1.0×10^{-21} cm^2 at 193 nm [53]. Only in the initial and final stages of the *e*-beam pulse, absorption by F_2 dominates when the population of argon excited states is small. The absorption coefficient is comparable to that measured by Mandl [23] and has a similar temporal behavior. However, the conditions there were considerably different: higher pressure (26 psi) and mostly neon (92.55 %) diluted with argon (7.3 %), at very low concentration of F_2 (0.15 %).

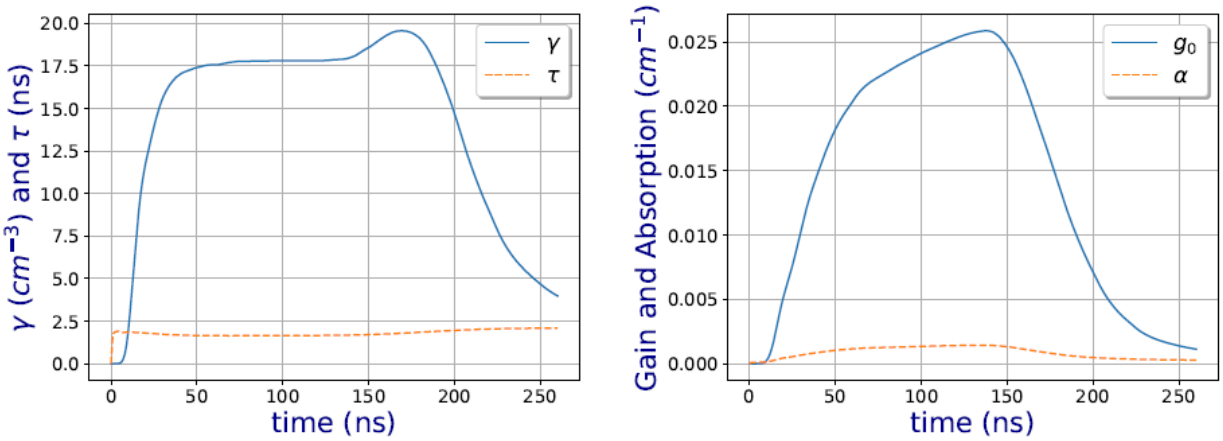

Fig. 8 —Coefficient γ and effective lifetime $\tau_{ArF^*(B)}$ (on the left), absorption coefficient α and small signal gain g_0 (on the right) for ArF^* oscillator. The *e*-beam power is 0.5 MW/cm^3. The total gas pressure is 12.5 psi and the gas composition is 0.5% of F_2 in Ar.

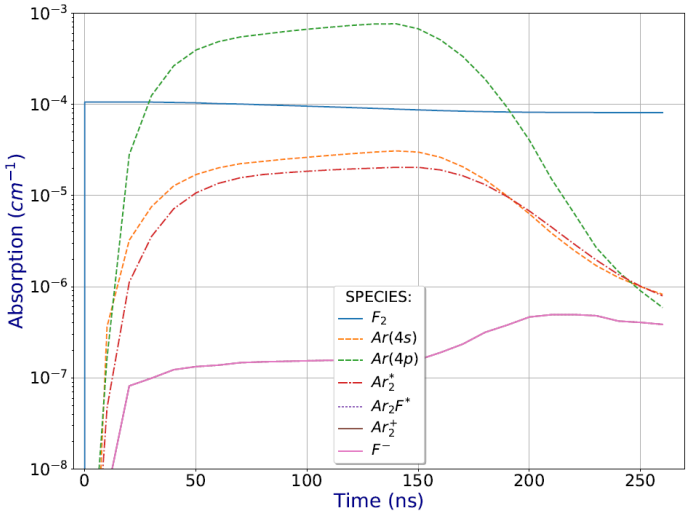

Figure 9 —Time-dependent absorption coefficients for *ArF** oscillator: partial contribution of different absorbers. The *e*-beam power is 0.5 MW/cm^3. The total gas pressure is 12.5 psi and the gas composition is 0.5% of F_2 in Ar.

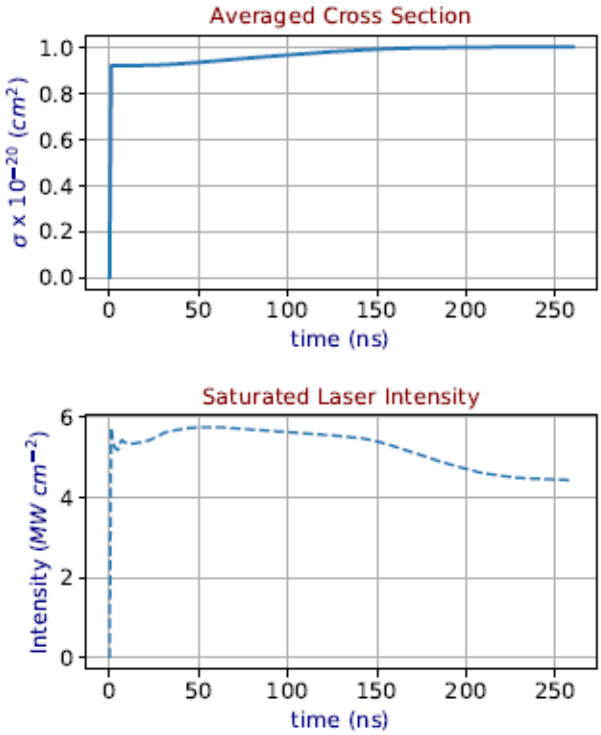

Fig. 10 —Single pass amplifier: absorption cross section (top) and saturated laser intensity I_{SAT} (bottom). The *e*-beam power is 0.5 MW/cm^3. The total gas pressure is 12.5 psi and the gas composition is 0.5% of F_2 in Ar.

The effective cross section for stimulated emission used in this work is $\sim 1 \times 10^{-16} cm^2$ (**Fig. 10**). Lee *et al.* adopted the value $2.75 \times 10^{-16} cm^2$ [26]. The saturation intensity (Formula 10) is ploted on the bottom for *e*-beam power is 0.5 MW/cm^3, total gas pressure is 12.5 psi, and gas composition is 0.5% of F_2 in Ar.

In relation to existing literature, Suda *et al*. [21] measured absorption coefficient $0.35\ \%\ /cm$ and small signal gain $0.6.4\ \%\ /cm$ obtained by Rigrod theory under the assumption of infinite V-T relaxation time. The peak extraction rate was 1.4 MW/cm^3 with power efficiency of 5.2 % at 4 atm Ne/Ar/F_2. In Mandl [23], for 200 ns e-beam duration and rise time of 25 ns, the intrinsic efficiency was 7.7 % and the power efficiency was 10 %. It was concluded, that at high pressures (2-5 atm) Ar/Ne/F_2 mixtures performed significantly better than Ar/F_2 mixtures, because the absorption shifts to wavelength 220 nm, and it was significantly smaller at 193 nm.

4. ENERGY BALANCE, LASER YIELD, AND ASE FOR ARF* LASER

The energy deposited in the gas by the electron beam is absorbed by the electrons and distributed among various channels. Part of the absorbed energy is emitted as radiation (ASE and lasing), while the other part remains as internal energy of the plasma. The energy terms are plotted in **Fig. 11** for e-beam energy $E_{BEAM}^{tot} = 6.12\ kJ$. For the first 30 ns of e-beam deposition the beam energy is spent for excitation and ionization of the background gas. It is stored primarily into excited states of *Ar* as internal energy (term denoted as E_{INT}). At later times the major portion of deposited energy is spent for gas heating in elastic collisions between electron and ground state atoms and molecules, which ends up as thermal energy of the gas denoted as $E_{TGH} = \frac{3}{2}\int N_g(z,t)k_B(T_g(z,t) - T_{g,0})dV$. There is an analogous energy term for the electrons, $E_{THE}(\mathrm{t}) = \frac{3}{2}\int N_e(z,t)k_B(T_e(z,t) - T_{e,0}(z,t))dV$, which is much smaller since the electron density N_e is several orders of magnitude smaller than the total gas density, N_g. Among the radiation channels, the lasing dominates the ASE. Here E_{LASR} is the energy spent in lasing and E_{LASRO} is the laser energy propagating in axial direction, which can be measured experimentally. The output laser energy reaches 90 J after 160 ns and remains almost constant till the end of the pulse. The energy spent for ASE is also plotted (term E_{ASE}). The ASE on axis also has subscript "0" added to it. The energy emitted as radiation from all other channels is denoted as E_{RAD}.

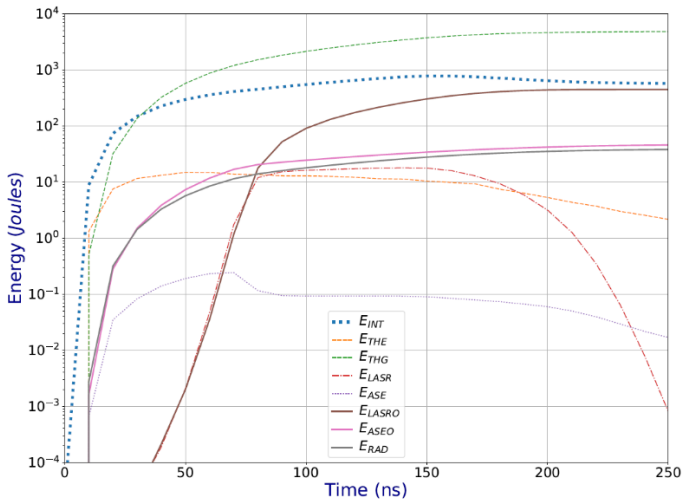

Fig. 11 —Energy terms as function of time for ArF* oscillator: The *e*-beam power deposition is 1 MW/cm^3, pulse beam shape shown in Figure 1. The total gas pressure is 12 psi with 0.5% of F_2 in Ar.

In general, amplified spontaneous emission occurs when a laser gain medium is pumped by an external *e*-beam source to produce a population inversion and subsequent lasing. ASE calculations are based on volumetrically discretized sets of cells with radiation emitted, transported and absorbed from each node of the cell as shown in **Fig. 12**, left. The figure on the right shows a section of the computational domain. ASE is collected and measured at the front side of the laser cavity by a detector, where the laser output is

also measured. The total ASE scalar flux $\Phi(k,\nu,t)$ for ArF* losses consists of a sum of stimulated emission and lasing photons at 193 nm:

$$\Phi(k,\nu,t) = \frac{I^{CF}_{LASER}[k,\nu,t]}{h\nu} + \frac{I^{CF}_{ASE}[k,\nu,t]}{h\nu}. \quad (18)$$

It is a function of axial zone k, frequency ν, and time t. Here I^{CF}_{LASER} is the laser intensity (subscript *LASER*) at the central frequency (superscript CF) and $I^{CF}_{ASE}[k,\nu,t]$ is the amplified spontaneous emission intensity (subscript ASE).

Perhaps the most important parameters used for guiding the experiments and monitoring the *Orestes* predictive capabilities are the laser yield and ASE energy. They are plotted in **Fig. 13** versus F_2 concentration for 1 MW/cm^3 *e*-beam power and total pressure of 12 psi (top) and 20 psi (bottom). This is the range of pressures the experiments are typically performed. Two models have been employed based on data in the **Appendix**: the 2021 model is based on the reaction rates in black and in the 2022 model, some of the reactions rates have been replaced with the formulas in red. The later were recommended in Ref. 33. The ASE is a small fraction of the laser yield, on the order of 1 %. At very low fractions of F_2 in Ar, the ASE-to-lasing energy ratio could be much larger, about 10 %. The laser yield is not very sensitive to total pressure, which should be close to 1 atm, but very sensitive to F_2 content: maximum lasing is calculated at $0.3 \pm 0.1\%$ F_2 in Ar. It was expected that the laser yield would increase with *e*-beam power deposition, however, there is an optimum *e*-beam power beyond which the lasing saturates because the ArF* molecules are dissociated by electron impact in the reaction $ArF^* + e \rightarrow Ar + F + e$. In particular, for e-beam power deposition 1 MW/cm^3, this reaction accounts for 35 % of the total destruction rate of the upper laser level ArF* (Table 3). Further increase of e-beam power would lead to even larger electron density and the above reaction will become the dominant loss mechanism of the upper laser level.

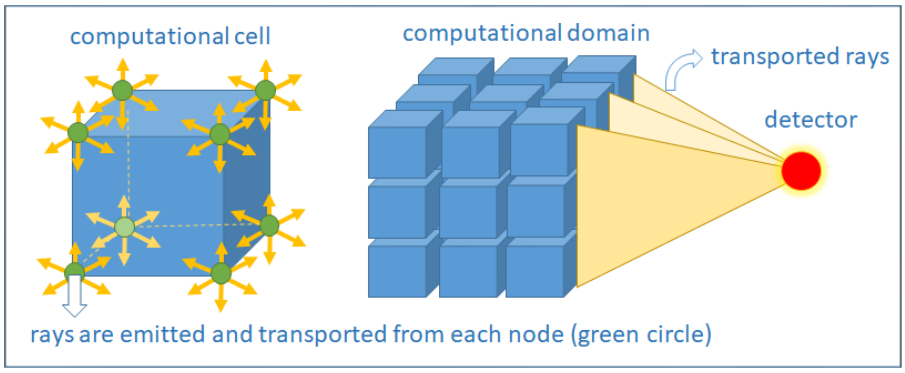

Fig. 12 — ASE radiation scheme: from each nod of the computational cell a user prescribed number of rays are emitted and transported. For illustration, on the right, rays for one of the nods are sketched. On axes computations and zone averaged results are used in most of the presented results. For example, a detector is situated in front of the laser cavity and plotted in red on the left. One should pay attention to the boundary conditions and data collection and interpretation.

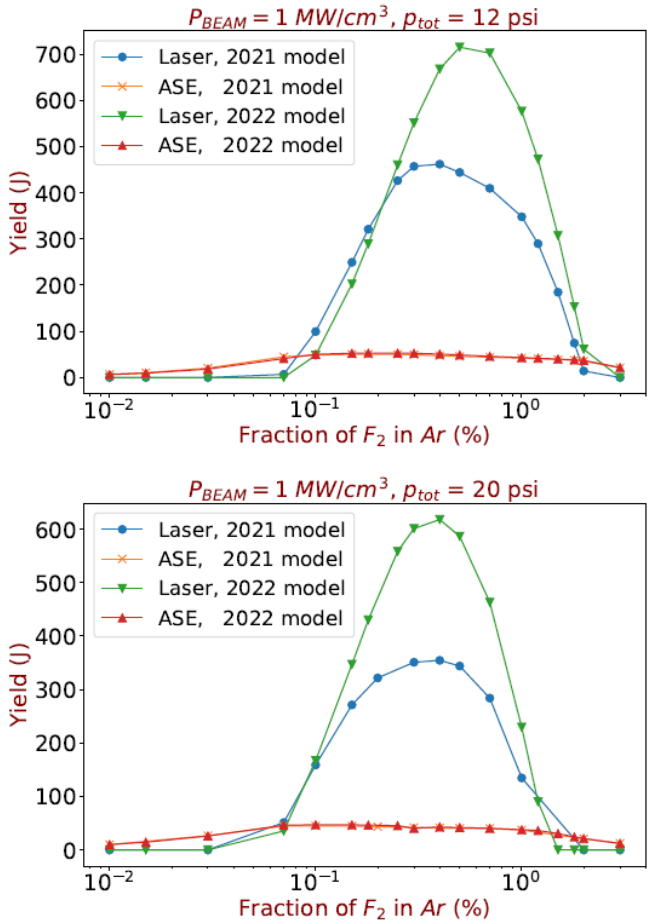

Fig. 13 —Laser yield and ASE for $ArF*$ oscillator at *e*-beam power of 1 MW/cm^3 in 15x30x100 cm^3 *e*-beam pumped volume and at different total gas pressure (12 and 20 psa) as a function of the fractional population of F_2 in Ar.

5. CONCLUSIONS

In this work we present the progress in modeling an electron beam pumped ArF^* laser and experiments on the NRL *Electra* facility. The modeling is based on NRL *Orestes* ArF^* suite of codes. Simulation results are compared both against experiments performed in-house and literature data. The key achievements of this work are:

- *Electra* has been successfully converted from $KrF*$ to ArF^* laser using different approaches and configurations described here in series of publications, Refs. [29], [30], [14], [32]. Orestes kinetics suite of codes has been rebuild from $KrF*$ to $ArF*$ using new data for the electron kinetics ([35]) and plasma-chemical reactions ([32] and [33]).
- We discussed different channels for creation and destruction of $ArF*$ molecules in order to determine their importance for laser energy efficiency and laser yield.
- In order to understand and improve the laser amplification through modeling, we explored different schemes of laser operation on *Electra*: single pass amplifier, double pass amplifier [29], and quadrupole oscillator [30]. Experimentally measured small signal gain, input intensity, saturated intensity, laser efficiency, and the ASE were used to benchmark the model. An intrinsic efficiency of 17.7 % was obtained for double pass amplifier with an output laser energy of 96 J [29]. Laser output energy as high

as 137 J was reported in Ref.[30] for double pass oscillator mode. Recently, the highest measured laser output, 200 J, was achieved at *e*-beam power deposition of $0.76\ MW/cm^3$, total gas pressure of $13\ psi$ and gas composition $0.5\%\ F_2$ in argon [to be published].

- Laser parameters have been studied as a function of *e*-beam power, gas pressure, and gas composition. It was found out that the laser yield is not very sensitive to total pressure, which should be close to $1\ atm$, but very sensitive to the F_2 content: maximum lasing is calculated at $0.3 \pm 0.1\%\ F_2$ in Ar.

These results are steps forward in building high efficiency $ArF*$ laser and for the laser scaling in future developments.

ACKNOWLEDGMENTS

The authors thank Laodice Granger and Areg Mangassarian for technical support. This work is supported by 6.1 Base Program and ARPA-E.

APPENDIX

Table A1 —Chemical Species

No:	Species:	Energy (eV):
1.	Ar	0.00
2.	Ar^*	11.65
3.	Ar^{**}	13.17
4.	Ar_2	0.00
5.	Ar_2^*	10.60
6.	F	0.82
7.	F_2	0.00
8.	F_2^*	11.57
9.	ArF^*	8.30
10.	Ar_2F^*	6.00
11.	Ar^+	15.76
12.	F_2^+	15.69
13.	Ar_2^+	14.53
14.	F^-	-2.58
15.	$electrons$	

Table A2 —Reactions with the *e*-beam electrons

Reactions:	Rates R (s^{-1}) and rate coefficients k $(cm^3 s^{-1})$:	References:
total ionization: $Ar + e\text{-beam} \longrightarrow Ar^+ + 2e$	$R_{Ar} = \gamma_{Ar} x_{Ar} R_{tot}^{ion}$ $\gamma_{Ar} = 1 + 0.57 x_{F_2}$	Petrov-2017
$F_2 + e\text{-beam} \longrightarrow F_2^+ + e$	$R_{F_2} = \gamma_{Ar} x_{F_2} R_{tot}^{ion}$ $\gamma_{F_2} = 0.467 + 0.25 x_{F_2}$	Petrov-2017
excitation: $Ar + e\text{-beam} \longrightarrow Ar^* + 2e$	$R_{Ar^*}^{exc} = \eta_{Ar^*}^{exc} R_{Ar}$ $\eta_{Ar^*}^{exc} = 0.155 + 0.120 e^{-180 x_{F_2}} P^{0.6}$ $+0.101 + 0.023 e^{-400 x_{F_2}} P^{1.2}$	Petrov-2017
$Ar + e\text{-beam} \longrightarrow Ar^{**} + 2e$	$R_{Ar^{**}}^{exc} = \eta_{Ar^{**}}^{exc} R_{Ar}$ $\eta_{Ar^{**}}^{exc} = 0.0898 + 0.004 x_{F_2} + 0.001 e^{-600 x_{F_2}} P^{1.5}$	Petrov-2017
$F_2 + e\text{-beam} \longrightarrow F_2^* + e$	$R_{F_2}^{exc} = \eta_{F_2}^{exc} R_{F_2}$ $\eta_{F_2}^{exc} = 0.48 + 0.075 e^{-250 x_{F_2}} P^{0.9}$	Petrov-2017
vibrational excitation: $F_2 + e\text{-beam} \longrightarrow F_2(vib) + e$	$R_{F_2}^{vib} = k_{F_2}^{vib} n_e n_{F_2}$ $k_{F_2}^{vib} = a + \frac{b}{1 + c\sqrt{x_{F_2}}}$ $a = 10^{-9}, b = (2 - 0.45 ln(P)) \times 10^{-9},$ $c = 50/(1 + 4P)$	k23, Petrov-2017
direct dissociation: $F_2 + e\text{-beam} \longrightarrow 2F + e$	$R_{F_2}^{dis} = k_{F_2}^{dis} n_e n_{F_2}$ $k_{F_2}^{dis} = \frac{a}{1 + (b + e x_{F_2})^{-1} + d\sqrt{x_{F_2}}}$ $a = (0.7 + 1.7 P^{0.35}) \times 10^{-9}, b = 0.2 + 0.15 P^{0.4},$ $c = \frac{10^3}{1+4P}$, $d = 10$	k25, Petrov-2017
dissociative attachment: $F_2 + e\text{-beam} \longrightarrow F^- + F$	$R_{F_2}^{att} = k_{F_2}^{att} n_e n_{F_2}$ $k_{F_2}^{att} = a + \frac{b}{1 + c\sqrt{x_{F_2}}}$ $a = 0.0, b = (2.3 - 0.5 ln(P)) \times 10^{-9},$ $c = 50/(1 + 4P)$	k24, Petrov-2017

Notes:

- normalized power deposition: $P = 2.0 * P_{BEAM}\,[MW/cm^3]/p[atm] + 10^{-3}$
- x_{F_2} is F_2 concentration and x_{Ar} is Ar concentration
- total ionization rate R_{tot}^{ion} for species $\alpha = Ar, F_2$ is summed over ionization, dissociation, and Auger ionization; $\gamma_\alpha = R_\alpha/(x_\alpha R_{tot}^{ion})$
- excitation-to-ionization ratio $\eta_{\alpha,k}^{\beta}$ is calculated for each species α, excitation level k, and type of process β as follow: $\eta_{\alpha,k}^{\beta} = R_{\alpha,k}^{\beta}/R_\alpha$

Table A3 —Reactions involving bulk electrons

Reactions:	Rates (units):	References:
electron impact atomic excitation:	rate in (cm^3s^{-1}), T_e in (eV)	
$Ar + e \longrightarrow Ar^* + e$	$3.7 \times 10^{-9} T_e^{0.74} e^{-17.4/T_e}$	Lee-1989
		k1, [Petrov-2017]
$Ar^* + e \longrightarrow Ar^{**} + e$	$8.1 \times 10^{-7} T_e^{-0.17} e^{-2.3/T_e}$	Kannari-1985
	$8.07 \times 10^{-7} T_e^{-0.17} e^{-1.51/T_e}$	k2, [Vriens-1980]
electron impact atomic de-excitation:	rate in (cm^3s^{-1}), T_e in (eV)	
$Ar^* + e \longrightarrow Ar + e$	$5.7 \times 10^{-9} T_e^{-0.17}$	k3, McGeoch-2018
$Ar^{**} + e \longrightarrow Ar + e$	$9.52 \times 10^{-10} T_e^{-0.17}$	k4, McGeoch-2018
$Ar^{**} + e \longrightarrow Ar^* + e$	$2.69 \times 10^{-7} T_e^{-0.17}$	k5, Vriens-1980
electron impact ionization:	rate in (cm^3s^{-1}), T_e in (eV)	
$Ar + e \longrightarrow Ar^+ + 2e$	$1.8 \times 10^{-8} T_e^{0.68} e^{-23.6/T_e}$	Lee-1989
		k6, [Petrov-2017]
$Ar^* + e \longrightarrow Ar^+ + 2e$	$5.2 \times 10^{-6} T_e^{0.67} e^{-6.27/T_e}$	Lee-1989
	$K_{ps} = \frac{3.65\times10^{-7} T_e^{0.83} e^{-4.06/T_e}}{1+1.86 T_e^{0.61}+0.206 T_e^{1.33}}$	k7, [Vriens-1980]
$Ar^{**} + e \longrightarrow Ar^+ + 2e$	$1.4 \times 10^{-7} T_e^{0.61} e^{-4.00/T_e}$	Lee-1989
	$K_{ps} = \frac{1.08\times10^{-6} T_e^{0.83} e^{-2.55/T_e}}{1+2.47 T_e^{0.61}+0.387 T_e^{1.33}}$	k8, [Vriens-1980]
$Ar_2^* + e \longrightarrow Ar_2^+ + 2e$	$6.8 \times 10^{-8} T_e^{0.7} e^{-5.25/T_e}$	Lee-1989
	$K_{ps} = \frac{4.53\times10^{-7} T_e^{0.83} e^{-3.7/T_e}}{1+1.97 T_e^{0.61}+0.23 T_e^{1.33}}$	k9, [Vriens-1980]
dissociative electron recombination:	(cm^3s^{-1})	
$Ar_2^+ + e \longrightarrow Ar^{**} + Ar$	$7.3 \times 10^{-8} T_e^{-0.67}$	k14, Mehr-1968
superelastic electron dissociation:	(cm^3s^{-1})	
$Ar_2^* + e \longrightarrow 2Ar + e$	5.0×10^{-8}	Lee-1989
		k17 estimated based on Neeser-1997
$Ar_2^* + e \longrightarrow Ar^* + Ar$	$5.0 \times 10^{-8} e^{-1.85/T_e}$	k16, estimated
		based on Vriens-1980
$ArF^* + e \longrightarrow Ar + F + e$	2.4×10^{-7}	k15, Lee-1989
$Ar_2F^* + e \longrightarrow 2Ar + F + e$	1.0×10^{-7}	Lee-1989

continue...

Reactions:	*Cross Sections/Rates:*	*References:*
electron attachment: $F + e \longrightarrow F^-$	$(cm^3 s^{-1})$ 1.0×10^{-12}	*Lee-1989*
inelastic dissociative attachment: $ArF^* + e \longrightarrow Ar^* + F^-$	$(cm^3 s^{-1})$ 3.0×10^{-8}	*this work* *k18 = 0, not used*
electron impact dissociation: $F_2 + e \longrightarrow 2F + e$	$(cm^3 s^{-1})$ 3.0×10^{-10}	*Lee-1989*
3-body electron-ion recombination: $Ar^+ + 2e \longrightarrow Ar^{**} + e$	*rate in* $(cm^6 s^{-1})$, T_e *in* (eV) $7.2 \times 10^{-27} T_e^{-4.5}$	*Kossyi-1992*

Note: k1 and k6 in McGeoch are for the e-beam electrons. These rates are valid from 0 to beam energy.

Table A4 —Reactions involving photons

Reactions:	*Cross Sections/Rates:*	*References:*
photo-absorption:	(cm^2)	
$Ar^* + h\nu_{B(v=0)} \longrightarrow Ar^+ + e$	3.5×10^{-20}	*Lee-1989*
		S1 [Duzy-1980]
$Ar^{**} + h\nu_{B(v=0)} \longrightarrow Ar^+ + e$	3.0×10^{-18}	*Lee-1989*
		S2 [Duzy-1980]
$F^- + h\nu_{B(v=0)} \longrightarrow F + e$	6.5×10^{-18}	*Lee-1989*
		Sfm [Mandl-1971]
$F_2 + h\nu_{B(v=0)} \longrightarrow 2F$	1.0×10^{-21}	*Lee-1989*
		Sf2 [Argüello-1995]
$Ar_2F^* + h\nu_{B(v=0)} \longrightarrow 2Ar + F$	5.0×10^{-19}	*Lee-1989*
	$\sigma(T_{vN}) = \sigma_{MAX} \times exp\left[\frac{T_{vN}}{50 + 0.1T_{vN}} - 10\right]$	*S6 [McGeoch-2019]*
		Estimate:
		$\sigma_{MAX} = 1 \times 10^{-17}$
		T_{vN} *from [McGeoch-2019]*
$Ar_2^+ + h\nu_{B(v=0)} \longrightarrow Ar^+ + Ar$	1.0×10^{-19}	*Lee-1989*
	$\sigma(T_{vC}) = \sigma_{MAX} \times exp\left[\frac{T_{vC}}{50 + 0.1T_{vC}} - 10\right]$	*S4 [McGeoch-2019]*
		Estimate:
		$\sigma_{MAX} = 1 \times 10^{-17}$
		T_{vC} *from [McGeoch-2019]*
$Ar_2^* + h\nu_{B(v=0)} \longrightarrow Ar_2^+ + e$	6.3×10^{-19}	*Lee-1989*
		S5 [Sauerbrey-1987]
$Ar_2^* + h\nu \longrightarrow Ar_2^{**} + Ar$	1.0×10^{-19}	*[McGeoch-2019]*
		S5a, estimate
stimulated emission:	(cm^2)	
$ArF^* + h\nu_{B(v=0)} \longrightarrow Ar + F + 2h\nu_{B(v=0)}$	1.9×10^{-16}	*McGeoch-2017*
		S7, [Dunning-1978]
$ArF^* + h\nu \longrightarrow Ar + F + 2h\nu$	1.9×10^{-16}	*Lee-1989*
spontaneous radiative decay rates:	(s^{-1})	
$ArF^* \longrightarrow Ar + F + h\nu_{B(v=0)}$	2.67×10^8	*Dunning-1978*
		–, [Dunning-1978]
$ArF^* \longrightarrow Ar + F + h\nu$	2.4×10^8	*Lee-1989*
		A7, [Dunning-1978]
$ArF^* \longrightarrow Ar + F + h\nu_X$	2.1×10^7	*Lee-1989*
$Ar_2F^* \longrightarrow 2Ar + F + h\nu_X$	4.3×10^6	*Lee-1989*
		A6, [Boewering-1982]
$Ar_2F^* \longrightarrow 2Ar + F + h\nu(126nm)$	3.5×10^5	*A5, [Millet-1982]*
$F_2^* \longrightarrow F_2 + h\nu_X$	2.7×10^8	*Lee-1989*

Reactions:	*Rates (units):*	*References:*
ion charge transfer:	$(cm^6 s^{-1})$	
$Ar^+ + 2Ar \longrightarrow Ar_2^+ + Ar$	2.1×10^{-31}	*Liu-1974*
	2.07×10^{-31}	*k22, Liu-1974*
		only from $Ar^+(^2P_{3/2})$
ArF^* *neutral relaxation:*	$(cm^3 s^{-1})$	
$ArF^* + Ar \longrightarrow 2Ar + F$	9.0×10^{-12}	*Kannari-1985*
		k26, Rokni-1977
$ArF^* + F \longrightarrow Ar + 2F$	1.0×10^{-12}	*Rokni-1977*
		k=0, not known
$ArF^* + F_2 \longrightarrow Ar + F + F_2$	1.8×10^{-9}	*Lee-1989*
	1.9×10^{-9}	*k27, Rokni-1977*
	$(cm^6 s^{-1})$	
$ArF^* + 2Ar \longrightarrow 3Ar + F$	5.0×10^{-32}	*Lee-1989*
$ArF^* + 2Ar \longrightarrow Ar_2F^* + Ar$	$1.62 \times 10^{-32} + 2.245 \times 10^{-21} T_g^{-3.9}$	*k28, Shui-1979*
		Chen-1978
Ar_2F^* *neutral relaxation*	$(cm^3 s^{-1})$	
$Ar_2F^* + F_2 \longrightarrow 2Ar + F + F_2$	2.0×10^{-10}	*Kannari-1985*
	2.05×10^{-10}	*k29, Marowsky-1982*
$Ar_2F^* + Ar \longrightarrow 3Ar + F$	2.2×10^{-14}	*Lee-1989*
$Ar_2F^* + Ar \longrightarrow ArF^* + 2Ar$	2.2×10^{-14}	*k30, Boewering-1982*
estimated products		*degeneracy weighted*
neutral particle reactions:	$(cm^3 s^{-1})$	
$Ar + Ar^{**} \longrightarrow Ar^* + Ar$	6.0×10^{-11}	*k36, Chang-1978*
$Ar + F_2^* \longrightarrow ArF^* + F$	1.0×10^{-9}	*this work*
$Ar^* + F_2 \longrightarrow ArF^* + F$	9.4×10^{-10}	*Chen-1978*
	1.0×10^{-9}	*k32, Chen-1979,*
		Chen-1978,
		Velazco-1976,
		degeneracy weighted
$Ar^{**} + F_2 \longrightarrow ArF^* + F$	1.0×10^{-9}	*this work*
		k33, estimated
$Ar_2^* + F \longrightarrow ArF^* + Ar$	1.0×10^{-9}	*this work*
		k=0, not known
$Ar_2^* + F_2 \longrightarrow ArF^* + Ar + F$	5.2×10^{-10}	*Lee-1989*
		k34, Chen-1978, Chen-1979
$Ar_2^* + F_2 \longrightarrow Ar_2F^* + F$	2.5×10^{-10}	*Wadt-1978*
		k35=0, Wadt-1978
$F_2^* + F_2 \longrightarrow F_2^* + 2F$	3.5×10^{-10}	*Lee-1989*
	$(cm^6 s^{-1})$	
$Ar^* + 2Ar \longrightarrow Ar_2^* + Ar$	1.1×10^{-32}	*Chen-1978*
		k31, Lorentz-1976
		degeneracy weighted

Table A5 —Heavy particles kinetics

Reactions:	*Rates (units):*	*References:*
Penning ionization:	$(cm^3 s^{-1})$	
$Ar^* + Ar^* \longrightarrow Ar^+ + e + Ar$	5.0×10^{-10}	*Kolokolov-1994*
	6.2×10^{-10}	*k10, Lee, Lieberman-1995*
$Ar^{**} + Ar^* \longrightarrow Ar^+ + e + Ar$	5.0×10^{-10}	*k11 Sigeneger-2016*
$Ar^{**} + Ar^{**} \longrightarrow Ar^+ + e + Ar$	5.0×10^{-10}	*k12*
$Ar_2^* + Ar_2^* \longrightarrow Ar_2^+ + e + 2Ar$	5.0×10^{-10}	*k13*
ion-ion recombination:	$(cm^3 s^{-1})$	
	$a_1 = \frac{N_{Ar}}{N_L}$	*Flannery-1978*
	Loschmidt's number: $N_L = 2.6868$	
	$a_2 = \frac{N_F - N_e}{10^{14}}$	
	$a_3 = 1.0$	*Bardsley-1980*
	$a_4 = \frac{1.1}{1.0 + \frac{a_2^{0.5}}{a_1^{0.4}}}$	*Morgan-1980*
$Ar^+ + F^- + (Ar) \longrightarrow ArF^* + (Ar)$	$\alpha = 3.4 \times 10^{-6}$	
	$k = 2\alpha \frac{a_1}{1.2} exp\left(1 - \frac{a_1}{1.2}\right) a_3 a_4$	
	$k = \frac{2.4N}{N^2 + 1.7} \times 3.417 \times 10^{-6}$	*k19, Flannery-1978*
	where $N \equiv a_1 = \frac{N_{Ar}}{N_L}$	
$Ar_2^+ + F^- + (Ar)$		
$\longrightarrow ArF^* + Ar + (Ar)$	$\alpha = 3.1 \times 10^{-6}$	
	$k = 2\alpha \frac{a_1}{1.6} exp\left(1 - \frac{a_1}{1.6}\right) a_3 a_4$	
	$k = \frac{2.65N}{N^2 + 1.7} \times 3.096 \times 10^{-6}$	*k20, Flannery-1978*
	where $N \equiv a_1 = \frac{N_{Ar}}{N_L}$	
$F_2^+ + F^- \longrightarrow 3F$	4.0×10^{-8}	*Kannari-1985*

REFERENCES

1*Topics in Applied Physics Excimer Lasers* vol. **30**, edited by Ch. K. Rhodes (Springer-Verlag-Berlin-Heidelberg-New York-Tokyo, 1984).

2 S. P. Obenschain, S. E. Bodner, D. Colombant, K. Gerber, R. H. Lehmberg, E. A. McLean, A. N. Mostovych, M. S. Pronko, C. J. Pawley, A. J. Schmitt, J. D. Sethian, V. Serlin, J. A. Stamper, C. A. Sullivan, J. P. Dahlburg, J. H. Gardner, Y. Chan, A. V. Deniz, J. Hardgrove, T. Lehecka, and M. Klapisch, "*The Nike KrF laser facility: Performance and initial target experiments*" Phys. Plasmas **3** (1996) 2098–2107.

3 S. P. Obenschain, R. Lehmberg, D. Kehne, F. Hegeler, M. Wolford, J. Sethian, J. Weaver, and M. Karasik"*High Energy Krypton Fluoride Lasers for Inertial Fusion*", Appl. Optics **54** (2015) pp. F103–F122.

4 J. D. Sethian, M. Friedman, J. L. Giuliani, JR., R. H. Lehmberg, S. P. Obenschain, P. Kepple, M. Wolford, F. Hegeler, S. B. Swanekamp, D. Weidenheimer, D. Welch, D. V. Rose, and S. Searles, "*Pulsed Power for a Rep-Rate, Electron Beam Pumped KrF Laser*" IEEE Trans. Plasma Sci **28** (2000) 1333–1337.

5 J. D. Sethian, D. G. Colombant, J. L. Giuliani, Jr., R. H. Lehmberg, M. C. Myers, S. P. Obenschain, A. J. Schmitt, J. Weaver, M. F. Wolford, F. Hegeler, M. Friedman, A. E. Robson, A. Bayramian, J. Caird, C. Ebbers, J. Latkowski, W. Hogan, W. R. Meier, L. J. Perkins, K. Schaffers, S. Abdel Kahlik, K. Schoonover, D. Sadowski, K. Boehm, L. Carlson, J. Pulsifer, F. Najmabadi, A. R. Raffray, M. S. Tillack, G. Kulcinski, J. P. Blanchard, T. Heltemes, A. Ibrahim, E. Marriott, G. Moses, R. Radell, M. Sawan, J. Santarius, G. Sviatoslavsky, S. Zenobia, N. M. Ghoniem, S. Sharafat, J. El-Awady, Q. Hu, C. Duty, K. Leonard, G. Romanoski, L. L. Snead, S. J. Zinkle, C. Gentile, W. Parsells, C. Prinksi, T. Kozub, T. Dodson, D. V. Rose, T. Renk, C. Olson, N. Alexander, M. A. Bozek, G. Flint, D. T. Goodin, J. Hund, R. Paguio, R. W. Petzoldt, D. G. Schroen, J. Sheliak, T. Bernat, D. Bittner, J. Karnes, N. Petta, J. Streit, D. Geller, J. K. Hoffer, M. W. McGeoch, S. C. Glidden, H. Sanders, D. Weidenheimer, D. Morton, I. D. Smith, M. Bobecia, D. Harding, T. Lehecka, S. B. Gilliam, S. M. Gidcumb, D. Forsythe, N. R. Parikh, S. O'Dell, and M. Gorensek, "*The science and technologies for fusion energy with lasers and direct-drive targets*" IEEE Trans. Plasma Sci. **38** (2010) 690–703.

6 M. Karasik, J. L. Weaver, Y. Aglitskiy, T. Watari, Y. Arikawa, T. Sakaiya, J. Oh, A. L. Velikovich, S. T. Zalesak, J. W. Bates, S. P. Obenschain, A. J. Schmitt, M. Murakami, and H. Azechiet, "*Acceleration to high velocities and heating by impact using Nike KrF laser*," Phys. Plasmas **17** (2010) 056317.

7 J. Weaver, R. Lehmberg, S. Obenschain, D. Kehne, and M. Wolford, "Spectral and far-field broadening due to stimulated rotational Raman scattering driven by the Nike krypton fluoride laser", Appl. Optics **56** (2017) 8618–8631.

8 F. Hegeler, D. V. Rose, M.C. Myers, J. D. Sethian, J. L Giuliani, M. F. Wolford, and M. Friedman, "*Efficient Electron Beam Deposition in the Gas Cell of the Electra Laser*", Phys. Plasmas **11** (2004) 5010–5021.

9 G. M. Petrov, J. L. Giuliani, and A. Dasgupta, "*Electron Energy Deposition in an Electron-Beam Pumped KrF Amplifier: Impact of Beam Power and Energy*", JAP **91** (2002) 2662–2677.

10 J. L. Giuliani, G. M. Petrov, and a. Dasgupta "*Electron Energy Deposition in an Electron-Beam Pumped KrF Amplifier: Impact of the Gas Composition*", JAP **92** (2002) 1200–1206.

11 R. H. Lehmberg and J. L. Giuliani, "*Simulation of Amplified Spontaneous Emission in High Gain* KrF *Laser Amplifiers*", JAP **94** (2003) 31–43.

12 R. H. Lehmberg, J. L. Giuliani, and A. J. Schmitt, "*Pulse Shaping and Energy Storage Capabilities of a Angularly Multiplexed KrF Laser Fusion Drivers*", J. Appl. Phys. **106** (2009) 023103.

13 J. W. Bates, A. J. Schmitt, M. Karasik, and S. T. Zalezak, "*Numerical Simulations of the Ablative Rayleigh-Taylor Instability in Planar Inertial-Confinement-Fusion Targets Using the FastRad3D code*", Phys. Plasmas **23** (2016) 122701.

14 S. P. Obenschain, A. J. Schmitt, J. W. Bates, M. F. Wolford, M. C. Myers, M. W. McGeoch, M. Karasik, and J. L. Weaver, "*Direct Drive with the Argon Fluoride Laser as a Path to High Fusion Gain with Sub-Megajoule Laser Energy*", Phil. Trans. R. Soc. A **378** (2020) 0031.

15 M. Rokni, J. H. Jacob, and J. A. Mangano "*Dominant Formation and Quenching Processes in E-Beam Pumped ArF* and KrF* Lasers*", PRA **16** (1977) 2216–2224.

16 M. Rokni, J. H. Jacob, J. A. Mangano, and R. Brochu, "*Formation and Quenching Kinetics of ArF*"*, APL **31** (1977) 79–82.

17 M. Rokni, J. A. Mangano, J. H. Jacob, and J. C. Hisa, "*Rare Gas Fluoride Lasers",* IEEE J. Quant. Electronics QE-14 **7** (1978) 464–481.

18 J. M. Hoffman, A. K. Hays, and G. C. Tisone, "*High-Power UV Noble-Halide Lasers*", APL **28** (1976) 538–539.

19 C. B. Edwards, F. O'Neill, and M. J. Shaw, "*60-ns e-Beam Excitation of Rare-Gas Halide Lasers*" APL **36** (1980) 617–620.

20 R. S. F. Chang, "*Electron-beam Pumped Kinetic Study of ArF*(B) State*" J. Chem. Phys. **78** (1983) 2210–2213.

21 A. Suda, M. Obara, and T. Fujioka "*Kinetic Studies of the Electron-Beam –Pumped ArF Laser Using an Ne/Ar/F2 Mixture*" Jpn. JAP **24** (1985) 1183–1188.

22 A. Suda, H. Kumagai, S. Izawa, and M. Obara, "*Comparative Study of Low-Pressure Rare-Gas Fluoride/Chloride Lasers Excited by a Short-Pulse Electron Beam*", JAP **64** (1988) 1720–1725.

23 A. Mandl, "*ArF Short-Pulse Excitation Studies*", JAP **59** (1986) 1435–1445.

24 P. J. Peters, I. H. T. Fierkens, and W. J. Witteman, "*Effect of Ne and Ar on the Performance of a High-Pressure ArF* Laser Pumped by a Small Coaxial Electron Beam*", APL **51** (1987) 883–885

25 Y-W. Lee, H. Kumagai, S. Ashidate, and M. Obara, "*High Efficiency Extraction of an Electron Beam Pumped ArF Laser Amplifier with an Atmospheric Pressure Ar-Rich Mixture*", APL **52** (1988) 1294–

26 Y-W. Lee, E. Matsui, F. Kannari, and M. Obara, "*Theoretical High-Efficiency Excitation Study of a Short-Pulse Electron-Beam-Pumped ArF Laser Amplifier with Atmospheric Pressure Ar-Rich Mixtures*", IEEE Trans Elec. Dev. **3** (1989) 2053–2065.

27 J. W. Glessner, M. J. McAuliffe, B. D. Smith, and K. B. Floyd,"Lasing of ArF with a microsecond Electron Beam", JAP **70** (1991) 4694–4696.

28 A. M. Boĭchenko, V. I. Derzhiev, A. G. Zhidkov, and S. I. Yakovlenko, "*Kinetic model of an ArF Laser*", Sov. J. Quntum Electronics **22** (1992) 444; A. M. Boĭchenko, V. I. Derzhiev, A. G. Zhidkov, and S. I. Yakovlenko "*Kinetics Model for Active Media of an ArF Laser*", Laser Physics **2** (1992) 210–220.

29 M. C. Myers, M. F. Wolford, A. J. Schmitt, Tz. B. Petrova, G. M. Petrov, J. L. Giuliani, M. McGeoch, and S. P. Obenschain, "*Development of an Electron Beam Pumped, Argon Fluoride Laser for Inertial Confinement Fusion*", PPS 2019 IEEE Conference Proceedings

30 M. F. Wolford, M. C. Myers, Tz. B. Petrova, J. L. Giuliani, T. J. Kessler, M. W. McGeoch, G. M. Petrov, A. J. Schmitt, T. A. Mehlhorn, and S. P. Obenschain, "*Development of a Broad Bandwidth* 193 *Nanometer Laser Driver for Inertial Confinement Fusion*", 11th International Conference on Inertial Fusion Science and Applications (IFSA 2019, Japan) and HEDP **20** (2020) 30061–6.

31 A. J. Schmitt and S. P. Obenschain, "*The importance of Laser Wavelength for Driving Inertial Confinement Fusion Targets, Part* I*: Basic Physics* and "*Part* II*: Target Design*", submitted to Phys. Plasmas

32 Tz. B. Petrova, M. F. Wolford, M. C. Myers, G. M. Petrov, J. L. Giuliani, M. W. McGeoch, A. J. Schmitt, and S. P. Obenschain, "*Modeling of an Electron-Beam Pumped ArF Laser*", IEEE ICOPS 2017, Atlantic City, NJ; "*Modeling of an Argon Fluoride Single Pass Amplifier*", 60th Annual Meeting of the APS DPP and 71st GEC, 2018, Portlant, Oregon; "*Plasma Chemistry Modeling of an Argon Fluoride Laser*", APS DPP 2018, Fort Lauderdale, Florida "*Plasma Kinetics Modeling of an e-beam Pumped ArF Laser*"APS DPP 2020, virtual conference.

33 M. W. McGeoch, Technical Notes, 2017, 2018, 2019.

34 Gu Zhi-yu, Wang Shao-yin, D. Proch, H. Weber, and K. L. Kompa, " *Kinetics Studied of Ar2F* in Fast Transverse-Discharge-Excited He-Ar-F2 Mixtures*,", Appl. Phys. B **31** (1983) 157161.

35 G. M. Petrov, M.F. Wolford, Tz. B. Petrova, J.L. Giuliani, and S. P. Obenschain, "*Production of Radical Species by Electron Beam Deposition in an ArF* Lasing Medium*", JAP **122** (2017) 133301.

36 F. Kannari, M. Obara, and T. Fujioka, "*An Advanced Kinetic Model of Electron Beam-Excited KrF Lasers Including theVibrational Relaxation in KrF*(B) and Collisional Mixing of KrF*(B,C)*", JAP **57** (1985) 4309–4322.

37 L. Vriens and A. H. M. Smeets, "*Cross sections and rate formulas for electron ionization, excitation, de-excitation, and total depopulation of excited states*", PRA 22 (1980) 940-951.

38 F. J. Mehr and M. A. Biondi, "*Electron-Temperature Dependence of Electron-Ion Recombi-nation in Argon*", Phys. Rev. **176** (1968) 322–326.

39 I. A. Kossyi, A. Yu. Kostinsky, A. A. Matveyev, and V. P. Silakov, "*Kinetics scheme of the non-equilibrium discharge in nitrogen-oxygen mixtures*", Plasma Sources Sci. Technol. 1 (1992) 207–220.

40 C. H. Chen, M. P. Payene, and J. P. Judish, *"Kinetic studies of ArF* and Ar2F* in proton-excited Ar-F2 mixtures*", J. Chem. Phys. **69** (1978) 1626–1635.

41 N. B. Kolokolov, A. A. Kudrjavtsev, and A. B. Blagoev, "*Interaction Processes With Creation of Fast Electrons in the Low Temperature Plasma*", Phys. Scripta **50** (1994) 371–402.

42 F. Sigeneger, M. M. Becker, R. Foest, and D. Loffhagen, "*Modelling of plasma generation and thin film Deposition by a non-thermal plasma jet at atmospheric pressure*", J. Phys D: Appl. Phys. **49** (2016) 345202.

43 W. F. Liu and D. C. Conway, "*Ion-Molecule Reaction Rates in Ar at* 296K", J. Chem. Phys. **60** (1974) 784–792.

44 M. R. Flannery and T. P. Yang, "*Ionic Recombination of Rare-Gas Atomic Ions X^+ with F^- in Dense Gas X*", Appl. Phys. Lett. **32** (1978) pp. 327–329.

45 J. N. Bardsley and J. M. Wadehra, "*Monte Carlo Simulation of Three-Body Ion-Ion Recombi-nation*", Chem. Phys. Lett. **72** (1980) 477–480.

46 W. L. Morgan, J. N. Bardsley, J. Lin, B. L. Whitten, "*Theory of Ion-Ion Recombination in Plasmas*", PRA **26** (1982) 1696–1703.

47 M. A. Gardner, A. M. Karo, and A. C. Wahl, "*Hartree-Fock Potential Energy Curves for the X $^2\Sigma^+$ and $^3\Pi$ States of NeF and ArF*",* J. Chem. Phys. **65** (1976) 1222–1224.

48 G. J. Hoffman and M. Colletto, "*An ab initio study of some noble gas monohalides*", J. Chem. Phys. **114** (2001) 2219–2227.

49 T. H. Dunning and P. J. Hay, "*The Covalent and Ionic States of the Rare Gas Monoflourides*" J. Chem. Phys. **69** (1978) 134–149.

50 W. W. Rigrod, "*Saturation Effects in High-Gain Lasers*", J. Appl. Phys. **36** (1965) 2487–2490.

51 A. M. Hunter, II and R. O. Hunter, JR., "*Bidirectional Amplification with Nonsaturable Absorption and Amplified Spontaneous Emission*", IEEE J. Quantum Electron. **QE-17** (1981) 1879–1887.

52 J. K. Rice, G. C. Tisone, and E. L. Patterson, "*Oscillator Performance and Energy Extraction from a KrF Laser Pumped by a High-Intensity Relativistic Electron Beam*", IEEE J. Quantum Electron. **16** (1980) 1315–1326.

53 G. A. Argüello, G. Balzer-Jöllenbeck, B. Jülicher, and H. Willner, *"Properties of Fluoroformyl Hypofluorite, FC(O)OF, Revisited",* Inorg. Chem. **34** (1995) 603–606.

54 C. Duzy and H. A. Hyman, "*Photoionization of Excited Rare Gas Atoms*". PRA **22** (1980) 1878–1883.

55 R. Sauerbrey, "*The Photoionization Cross Section of the Rg_2^*, [$^3\Sigma_u^+$] excimer states for N_2^*, Ar_2^*,* and *Kr_2^**", IEEE Quantum Electronics Letters **QE-23** (1987) 5–8.

56 A. Mandl, "*Electron Photodetachment Cross Section of the Negative Ion of Fluorine*", PRA **3** (1971) 251–255.

57 Tz. B. Petrova, G. M. Petrov, M. F. Wolford, J. L. Giuliani, H. D. Ladouceur, M. C. Myers, and J. D. Sethian, "*Effective NOx Remediation from a Surrogate Flue Gas Using the US NRL Electra Electron Beam Facility*", Phys. Plasmas **24** (2017) 023501.

58 S. Nagai, M. Sakai, H. Furuhashi, A. Kono, T, Goto, and Y. Uchida, "*Measurements of Temporal Behavior of Electron Density in a Discharge-Pumped ArF Excimer Laser*", IEEE J. Quant. Electronics **34** (1998) 40–46.

59 W. L. Morgan, "*A Critical Evaluation of Low-Energy Electron Impact Cross Sections for Plasma Processing Modeling*: I: *C*2, *F*2, and *HCl*", Plasma Chem. Plasma Process. **12** (1992) 449 –476.

60 M.C. Myers, M. F. Wolford, A. J. Schmitt, Tz. B. Petrova, G. M. Petrov, J. L. Giuliani, M. McGeoch, and S. P. Obenschain, 48th Annual Anomalous Conference, Bar Harbor, ME, July 8-13, 2018.

61 J. L. Giuliani, "*Technical Notes on Laser Oscillators and Amplifiers*", 2002, NRL.

62 R. G. Adams and M. M. Dillon, "*Narrow Linewidth Gain Measurements in KrF and ArF Excimer Amplifiers Pumped Longitudinally by High-Power Electrons*", JAP **70** (1991) 4073–4081.